ADDITIVE MANUFACTURING OF IRON-COBALT ALLOY FOR ELECTRIC MOTORS

Thesis

Submitted to

The School of Engineering of the

UNIVERSITY OF DAYTON

In Partial Fulfilment of the Requirements for

The Degree of

Master of Science in Materials Engineering

By

Derek Michael Smith

Dayton, OH

December 2021

ADDITIVE MANUFACTURING OF IRON-COBALT ALLOY FOR ELECTRIC MOTORS

Name: Smith, Derek Michael

APPROVED BY:

Dr. Donald Klosterman
Advisory Committee Chairman
Torley Endowed Chair in Composite Materials
Associate Professor
School of Engineering

Dr. Li Cao
Committee Member
Associate Professor
School of Engineering

Dr. Zafer Turgut
Committee Member
Senior Scientist
Air Force Research Laboratory

Robert J. Wilkens, Ph.D., P.E.
Associate Dean for Research and Innovation
Professor
School of Engineering

Margaret Pinnell, Ph.D.
Interim Dean, School of Engineering

ABSTRACT

ADDITIVE MANUFACTURING OF IRON-COBALT ALLOY FOR ELECTRIC MOTORS

Name: Smith, Derek Michael
University of Dayton

Advisor: Dr. Donald Klosterman

Additive Manufacturing (AM) is a rapidly developing field that offers new possibilities for manufacturing with materials that are difficult to process with traditional manufacturing methods. This report will examine the application of selective laser melting in making magnetic cores out of Hiperco 50. The iron-cobalt family of alloys is known to offer the best magnetic properties of all soft magnetic materials but is extremely brittle. Additive manufacturing offers the opportunity to make high quality magnetic cores in unique geometries that traditional manufacturing is unable to replicate.

To test the viability of this process three types of test specimens were built out of Hiperco 50 powder to examine key material properties. First 1 cm^3 cube specimens were built to measure the density of the final parts, and they were also used to examine the porosity and microstructure. The second type of specimens were tensile bars, built in both vertical and horizontal orientations with respect to the build plate, to examine the mechanical properties of the final parts as well as the impact of build orientation. The final test specimens were magnetic toroids, comprised of cores to be wound with copper magnet wire and tested for magnetic permeability and remanence. Half of these specimens were also subjected to a final magnetic heat treatment cycle, which was the same as the cycle used for traditionally manufactured Hiperco 50 components, in order to determine the change in performance.

These AM fabricated specimens showed a 1-5% decrease in density from traditionally manufactured Hiperco 50 parts, with the build parameters being the largest deciding factor of final density and porosity. These parts also had a poorly defined grain structure until subjected to a magnetic heat treatment. After undergoing the recommended heat-treatment, niobium precipitates were observed along the newly defined grain boundaries. However, there was a severe drop in mechanical performance, and a minor increase in magnetic properties. Overall, the magnetic performance of all specimens was considerably worse than traditional Hiperco 50 cores, exhibiting permeabilities orders of magnitude lower than the traditionally manufactured counterparts. The cause for this could be attributed to the porosity of the final specimens, which would disrupt uniform magnetic field lines forming around the toroid with internal fields opposing magnetization.

With the high cost per part and poor observed magnetic performance, selective laser melting is not recommended as a replacement for traditional methods without significant further development. The data gathered here indicates that while Hiperco 50 did retain some of its magnetic properties, truly unique geometries must be necessary to make the trade-off in performance worth the performance drop, cost, and time investment to make additive manufacturing a serious consideration.

Dedicated to my parents, Kevin and Jackie Smith. Without their support none of this would be possible.

ACKNOWLEDGEMENTS

First and foremost, I'd like to thank John Middendorf and his team at Arctos Technology Solutions, whose donation of time, experience, and equipment made this project possible. I'm also extremely grateful to my advisors Don Klosterman at the University of Dayton, and Justin Delmar and Zafer Turgut of the Air Force Research Lab Aerospace Systems Directorate. Their guidance and advice helped me manage an undertaking of this degree for the first time. I'd also like to thank Dr. Robyn Bradford and Dr. Li Cao at the University of Dayton, who greatly aided me in my sample preparation and microscopy analysis on campus and provided guidance in writing and editing this work. For their help in training me on the equipment and machinery utilized at AFRL I'd like to offer special thanks to Ken McFarlane, Jacob Lawson, Michael McCleod, and James Green. Additionally, I'd like to express my gratitude to Mark Benedict, Mike Velez, Phil Blosser, Dale Osborne, and Ken Isbil at the Materials and Manufacturing Directorate, who provided access and expertise with much of the equipment used throughout this report. I would also like to thank Gregg Temple with Winston Heat Treating for his time and experience with the heat treatment of my samples.

TABLE OF CONTENTS

LIST OF FIGURES

LIST OF TABLES

LIST OF ABBREVIATIONS AND NOTATIONS

AM- Additive Manufacturing

LENS- Laser Engineered Net Shaping

SLM- Selective Laser Melting

EM- Electromagnetic

Fe- Iron

Co- Cobalt

V- Vanadium

Nb- Niobium

UDRI- University of Dayton Research Institute

AFRL- Air Force Research Laboratory

UTS- Ultimate Tensile Strength

PTFE- Polytetrafluoroethylene AKA Teflon

F- Focused

U- Unfocused

AB- As-Built

HT- Heat-Treated/Annealed

S- Sanded Surface

SE- Sanded Edges

CHAPTER 1

INTRODUCTION

With the continuous and rapid advancement of additive manufacturing (AM) technology over the past three decades there exists a unique possibility to reexamine which industries may benefit from a new approach to manufacturing. While the AM industry continues to establish itself in creating structural parts and quickly producing prototypes, one area of limited investigation so far has been the use of AM techniques to produce magnetic components. The field of AM allows for novel geometries, new alloys that are difficult to use in traditional manufacturing techniques, and fine control of a material's microstructure throughout a build. This offers the potential to revolutionize motor performance by allowing for complex geometries and microstructures to be created that were not possible or practical before.

There are two AM techniques of particular note in relation to the construction of soft magnetic components: Laser Engineered Net Shaping (LENS) and Selective Laser Melting (SLM). While LENS is not the focus of this report it is a promising field of study. LENS melts the powder before it is propelled to the surface via an inert gas jet, keeping the feed system in position while moving the build surface around to create the scan pattern. SLM, also known as Laser Powder Bed Diffusion, is the more traditional AM technique where the build surface is covered with layers of powder and a laser traces a path across the surface to locally melt the powder in the desired shape. Both of these methods allow for interesting new part geometries when building a three-dimensional part.

A material that could greatly benefit from the differing manufacturing advantages afforded by AM is the iron-cobalt binary system. Traditionally pure iron-cobalt is incredibly

difficult to work with as it is an extremely brittle material. Without extreme care, hot and cold working techniques can lead to cracking which will diminish the physical and magnetic properties of the final part. The FeCo system offers the highest magnetic permeability of any known material making it an excellent choice for compact, high torque motor applications. To combat the fragility of the binary alloy there have been many ternary additives selected to improve the workability of the material without sacrificing too much of the outstanding magnetic properties. This report will focus on one of those alloys, Hiperco 50, with a 2 wt% vanadium ternary addition that is one of the most commonly used FeCo alloys.

This report will investigate the performance of Hiperco 50 parts constructed via AM with particular interest in the change in density, tensile properties, and magnetism when compared to traditionally manufactured Hiperco 50. Recently published research into AM Hiperco parts will also be reported on. This will allow for the investigation of the relationship between processing, conditioning, and the measured material properties, as well as any unintended factors that could impact the performance of AM Hiperco 50 as a magnetic core material.

CHAPTER 2

LITERATURE REVIEW

2.1 RESEARCH GOALS

The primary goal for this study was to determine the viability of SLM and heat treatment to balance magnetic and structural properties of a commercially available metal powder, Hiperco 50 (developed by Carpenter Technology Corp.), to create electric motor components. SLM will be used to create test specimens to measure the magnetic, physical, and mechanical properties of AM processed Hiperco with and without heat treatment. These results will be compared to the manufacturer specification as well as results from recent literature, including parts made from both AM techniques and traditional metal working processes. The rotor and stator components of electric motors rely on soft ferromagnets to operate via insulated copper coils. The key material properties of concern for electric motor components are density, tensile strength, permeability, coercivity, and saturation. In support of this research, a literature search was undertaken to review various technical areas including electromagnetism and motors, additive manufacturing, and the properties of Hiperco 50.

2.2 ELECTROMAGNETISM

Electromagnetism is one of the four fundamental forces of nature, being comprised of the electric force (the attraction/repulsion of electrical charges) and the magnetic force (the attraction/repulsion resulting from the movement of electrical charges). While these component forces have been observed and utilized *individually* for hundreds or possibly thousands of years, it was not until Hans Christian Oersted [1, pg1-2] created the first electromagnet in 1825 that the

connection between the two was established. Since then, society has become reliant upon devices that utilize electromagnetic (EM) forces to complete everyday tasks, from transmitting power from power plants to our homes, to starting our cars, to communicating over long distances. The electromagnetic force is most easily understood in traditional electromechanical devices such as generators or motors.

2.2.1 FERROMAGNETISM

The phenomenon of ferromagnetism refers to a material's ability to have a magnetic field induced in it via exposure to an applied magnetic field. Ferromagnetic materials have been used by humanity for nearly as long as we have known about magnetism. The first human-made magnets, which occurred after discovering the naturally occurring magnetic material magnetite (Fe_3O_4), were iron bars rubbed with this magnetic mineral [1, pg 1]. These early human-made magnets were used as compasses which is the source of the North-South pole terminology used to differentiate magnetic poles to this day. When allowed to freely float in a magnetic field (such as the Earth's naturally occurring field) a magnet's northern magnetic pole aligns to Earth's magnetic north. While these primitive ferromagnets were indeed very useful to our ancestors in navigation and primitive lifting/locking devices, they required significant effort to produce and were usually permanent magnets. With the advent of the electromagnet, in which the magnetic field can be turned on and off, the increased power and versatility of human-made magnets allowed for a much wider application of magnets.

Ferromagnetic materials are typically defined from other types of magnetism by two parameters: susceptibility and permeability. Susceptibility (κ) is the quotient of the induced magnetic moment (M) and the applied magnetic field (H). For ferromagnetic materials susceptibility is generally high, meaning that for a small, applied field there will be a large response in the induced magnetic moment [1, p17]. In similar fashion to susceptibility, permeability (μ) is the quotient of total induced magnetic flux density (B) and the applied

magnetic field strength (H), μ=B/H, and it represents the change in field strength of the resultant field of a material relative to the applied field. Again, for ferromagnetic materials this value is generally large, indicating that for small input fields the induced flux response is very large. These two properties are related to each other via the following equation [1, pg 17]:

$$\mu = 1+4\pi\kappa \tag{1}$$

Ferromagnetic materials can maintain their magnetic moments outside of an external field and are classified in two different categories based on how easily they can be magnetized/demagnetized: hard and soft. The difference between these two types of ferromagnets can be seen on a hysteresis plot, a form of expanded magnetization curve. The hysteresis plot displays the applied magnetic field on the material against the resulting magnetic flux density inside the material. An example hysteresis plot can be seen below in Figure 1, with a representation of a hard magnet depicted in orange and a soft magnet in blue.

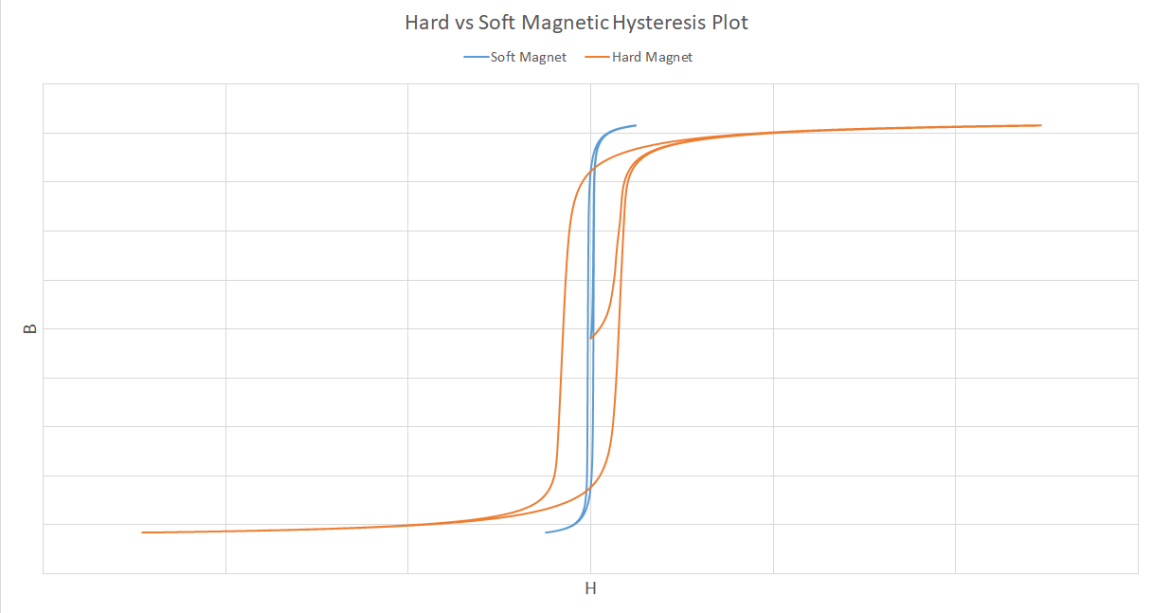

Figure 1: Sample Hysteresis Plot of Hard/Soft Magnets

Hard ferromagnets are characterized by how difficult they are to magnetize, their energy product $(BH)_{max}$,[2] and the high magnitude of the magnetic field to which they need to be exposed to achieve saturation (M_s). This is representative of a large area under their hysteresis curve, meaning that they maintain their magnetization exceptionally well. Typical hard ferromagnet applications include bar and horseshoe magnets, speaker magnetics, measuring devices, MRI machines, and computers.

Soft ferromagnets on the other hand need to be quickly magnetized and demagnetized for their applications in rapidly alternating EM fields. This means that lower field strengths can be applied to generate magnetic fields quickly and then removed to end the magnetization. The combination of high magnetic flux resulting from low applied field strength means that soft ferromagnets can convert between electrical and magnetic energy with little energy lost as heat. This is critical in motor/generator applications as increasing the heat of the motor decreases the electrical and magnetic properties of its components, namely magnetization, resulting in a compounding decrease in efficiency through continued use.

To understand what makes ferromagnets such excellent magnetic materials one must understand two distinct properties of ferromagnets as discovered by Pierre Weiss and described by the Weiss Theory of Ferromagnetism, Domain Theory, or Molecular Field Theory [1, pg 119]. The first property of ferromagnets is their spontaneous magnetization: Weiss postulated that ferromagnets when left on their own (i.e. outside of magnetic fields) will approach magnetic saturation. To explain how this tendency for spontaneous magnetization does not yield active magnetic fields around all ferromagnets Weiss surmised that each ferromagnet is composed of multiple saturated regions called domains. This does not mean that ferromagnetic materials will produce a net magnetic field spontaneously, but rather that inside of the ferromagnet there are multiple opposing and misaligned magnetic domains that reach magnetic saturation [1, pg 119]. Thus, when exposing a ferromagnet to a magnetic field the field only grows and aligns these

domains in such a way as to first create a unified magnetization and then align it in the direction of the applied field.

To explain why these materials only self-magnetize until their saturation point one must consider both the magnetization curve (M vs H) and the molecular field response to a given magnetization, where γ is the molecular field coefficient (H vs H_m):

$$H_m = \gamma M \tag{2}$$

There are two points at which these equations are equal which serve as resting points for increasing magnetization, at 0 magnetization and at magnetic saturation (M_s). Due to the presence of Earth's magnetic field, there are very few circumstances in which a ferromagnet will rest at a 0 magnetization point. Thus, as its magnetization increases, the molecular field responds according to the above equation increasing the net magnetic field acting on the material:

$$H_t = H+H_m \tag{3}$$

This increase in the field strength then increases the magnetization and the process repeats itself until the saturation magnetization is reached where any further increase in H or M leads to a weakening of the molecular field response.

It should be noted, however, that magnetism is not a constant material property based on composition alone. Properties that can affect the magnetic performance of a given material include temperature, grain structure, and orientation.

With increasing temperature, ferromagnetic materials trend towards becoming paramagnetic (low susceptibility and low permeability). For reference, a paramagnetic material only increases the applied field by ~0.02% while ferromagnets at their peak magnetic performance can yield increases on the order of 10^3 to 10^6 times the applied field strength [1, pg 12]. This behavior transitions fully into paramagnetic behavior at the material's Curie

Temperature (T_c). For the scope of this research, the Curie temperature of most materials is well beyond the operating temperatures of the electric motors in question, but there is still a decrease in the induced field strength with increasing temperature. For example, between 0K and 293K iron loses approximately 2.6% magnetization (a decrease of 45 Gauss) and cobalt sees a similar decrease of 3.3% (46 Gauss). While these amounts aren't large on their own, they are compounded with other types of loss leading to noticeable decreases in performance [3, pg 4].

The grain structure of a ferromagnetic material can also noticeably impact its magnetic performance. The optimal size of grains in a ferromagnet depends on the magnitude of the magnetic field to which it is exposed. For example, the permeability of electrical steel was found to improve with larger grains (~210 μm) in weak magnetic fields while much smaller grains (~50 μm) were found to be ideal in stronger fields [4]. This is due to the increasing impact of the domain wall rotations in smaller gains.

The final material property that drives the performance of ferromagnets is orientation or anisotropy. Generally speaking, there are three directions of magnetization inside a crystal, which are referred to as easy, medium, and hard. The orientation of these directions depends primarily on the crystal structure of the material in question, for this report the BCC iron-cobalt system is of primary concern. The "easy" direction is the direction that requires the lowest applied field strength to reach saturation; this is also the state in which self-saturating domains will naturally appear. For the BCC structure the easy direction is <100>, and the difficulty of saturation increases with a longer path through the crystal. Therefore, the <110> direction is medium and <111> is hard. The "medium" and "hard" directions require an increasing applied field magnitude to achieve saturation magnetization, as the natural state of the "easy" direction resists rotating domains away from it [1, 209].

Note that this summary of ferromagnetism does not include all possible methods of magnetic losses (i.e. effects that impede the transition of applied EM fields to induced EM fields),

nor does it discuss the distinction between Molecular Field Theory and the more widely accepted Band Theory when it comes to the behavior of the electrons of individual atoms/crystals. This was deemed to be outside of the scope of this report. For further analysis of the phenomenon of ferromagnetism refer to Cullity's Introduction to Magnetic Materials [1] or volume 18 of the Encyclopedia of Physics: Ferromagnetism [3].

2.2.2 ELECTRIC MOTORS

One of the most prevalent uses of ferromagnetic materials in the modern world is as a core component of electric motors. These motors drive everything from the cooling fans in computers to electric cars. Typically, electric motors consist of two key ferromagnetic components: the rotor and stator, which usually are laminates of thin layers of ferromagnetic material wound with electrically insulated copper wire.

There are many different classifications for electric motors, but they all operate on the same principle: rotational motion is created as a result of imbalanced magnetic forces. This imbalance can be due to the alternating of the source current as in AC motors, or in interruptions to the current entering the coils as in DC motors. By far the most common variety of DC motor on the market now is the brushless motor, which uses a combination of permanent magnets and electromagnets to control the speed of the device. The electromagnets use the magnitude of their applied voltage and the interval between coil activation/deactivation to rotate the permanent magnets of the rotor. To help reduce the losses when inducing magnetism in the cores of the stator, most cores are laminates of insulated layers of ferromagnetic core material. A simple diagram of a brushless DC motor can be seen below in Figure 2.

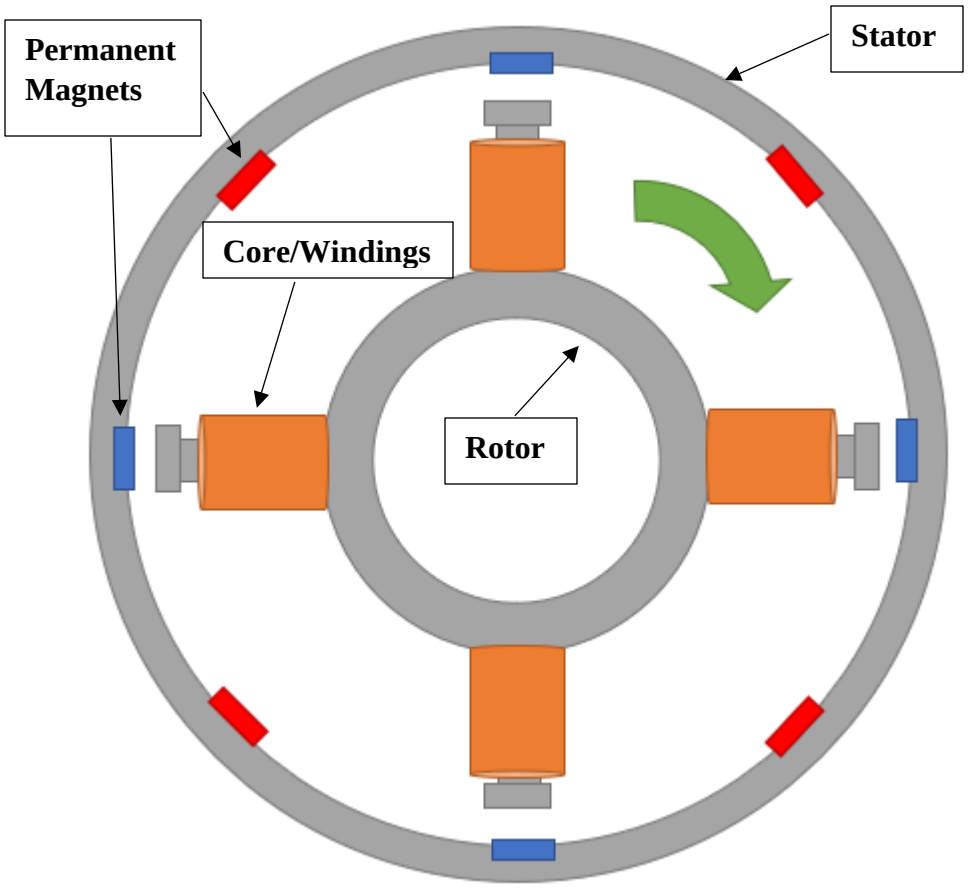

Figure 2: DC Motor Diagram

When a core material produces a magnetic field as the result of induction coils there is a response to the changing flux in which the applied electric current creates a magnetic field, which induces a magnetic field in the core, which then develops its own internal electric field proportional to the applied electric current. It is on this principle that transformers operate, but the induced electric field is in a secondary winding material rather than the core material. This induced core current has no outlet in motor applications and is generated in a direction in opposition to the applied fields. This results in a net decrease in flux as well as an increase in temperature, decreasing the overall performance of the motor. This heat loss is controlled by the induced current as well as the resistance that current encounters along its path through the core

and is equal to I^2R (the calculation of the magnitude of the loss) or eddy current loss. Since the performance of the motor will dictate the need for the applied current, the simplest way to reduce eddy current losses is to reduce the length/total resistance that the induced current will encounter along its path. As the magnitude of the magnetic field generated by a given core is related chiefly to its size rather than any internal continuity, a good core material can be made in a laminate form and exhibit little observable performance loss.

Another area in which loss will occur in an electric motor is hysteresis loss, which refers to the loss involved in magnetizing/demagnetizing a material. It is referred to as hysteresis loss as it is directly proportional to the area under the curve of a hysteresis plot of magnetizing a material:

$$W_h = \text{B,H Area}/4\pi \tag{4}$$

This loss is constant for the material and not dependent upon how the motor is performing, unlike eddy current loss. While this material hysteresis may be described as a constant factor, there is another form of hysteresis loss that becomes relevant in the rapid rotation and domain shifting of motors known as rotational hysteresis loss, W_r. Rotational hysteresis refers to the losses that occur from constantly rotating domains inside a core material. Contrary to the creation of permanent magnets, motors don't always necessarily fully align to any domain that they are exposed to, but rather expand and contract the domain areas best aligned with the applied field at lower field strengths [1, pg 508]. As these domains move back and forth across the material, they will inevitably become stuck on defects in the material, stretching until the pinning energy is released as heat and a small eddy current. This effect is known as Barkhausen Noise or Domain Wall Pinning [1, pg 508], and directly related to the torque and applied angle of the field. If a material does reach saturation in a single domain direction though, the rotational hysteresis goes to zero and the magnetic anisotropy has a greater sway over the material performance [1, pg 510].

2.3 ADDITIVE MANUFACTURING OF METAL COMPONENTS

As the field of AM expands, so too does the search for novel applications of the technology. Additive manufacturing allows for rapid construction of unique designs and geometries that are impossible to achieve via other more traditional methods, as well as the possibility of layer by layer control of properties in a single part.

These advantages usually come at a greatly increased cost of the individual part (although this may be offset by the reduction or elimination of tooling costs), very often reduced mechanical properties of the final part (depending on orientation relative to the build), and the continued reliance on traditional methods to finish parts due to surface roughness. While AM reduces the time required to create a single part or small batch, there is little recovery in costs to be made from larger orders as there is little or no investment in reusable infrastructure such as dies or stamps. For the time being, use of AM for motor applications is expected to be best applied to prototyping, small lot production of specialty motors, and replacement of damaged components in old motors that are no longer produced.

2.3.1 SELECTIVE LASER MELTING (SLM)

Selective Laser Melting (SLM) is the main additive manufacturing method focused on in this report, Figure 3 below offers a simplified overview of the system. SLM uses a sharply focused high-power laser beam to entirely melt small areas of metal powder in a large powder bed. The laser is fired from a position above the powder bed and is directed to the build area by a series of mirrors and lenses. Typical focal point spot sizes for AM applications range from 50 to 180 μm and laser powers range of 20 W to 1 KW [5]. The melt pool solidifies quickly leaving a solid metal layer to continue to build on with unique rapidly cooled microstructures. As the solidified pattern in each layer is completed, the work surface is lowered and a new layer of powder is added from a secondary reservoir to maintain constant working distance for the laser.

While this method of complete powder melting does allow for high density parts to be manufactured (99% density), it requires a precise selection of parameters to find a balance between speed and performance [6, 8, 9]. The key equation used to help develop laser parameters is given in Equation 5 below, where P_L is the power of the laser, v_s is the speed of the laser over the build surface, h_s is the spacing between the planned laser paths, and D_S is the depth of the powder applied to each layer.

$$E_v = P_L/(v_s h_s D_S) \tag{5}$$

E_v is called the volume energy density which is used to represent the amount of energy put into the powder bed per unit volume in the melting of one layer-pass [5]. While this has been criticized as an oversimplification of the actual mechanics of the melt pool during the SLM process, a discussion of other phenomena remains outside of the scope of this report [7].

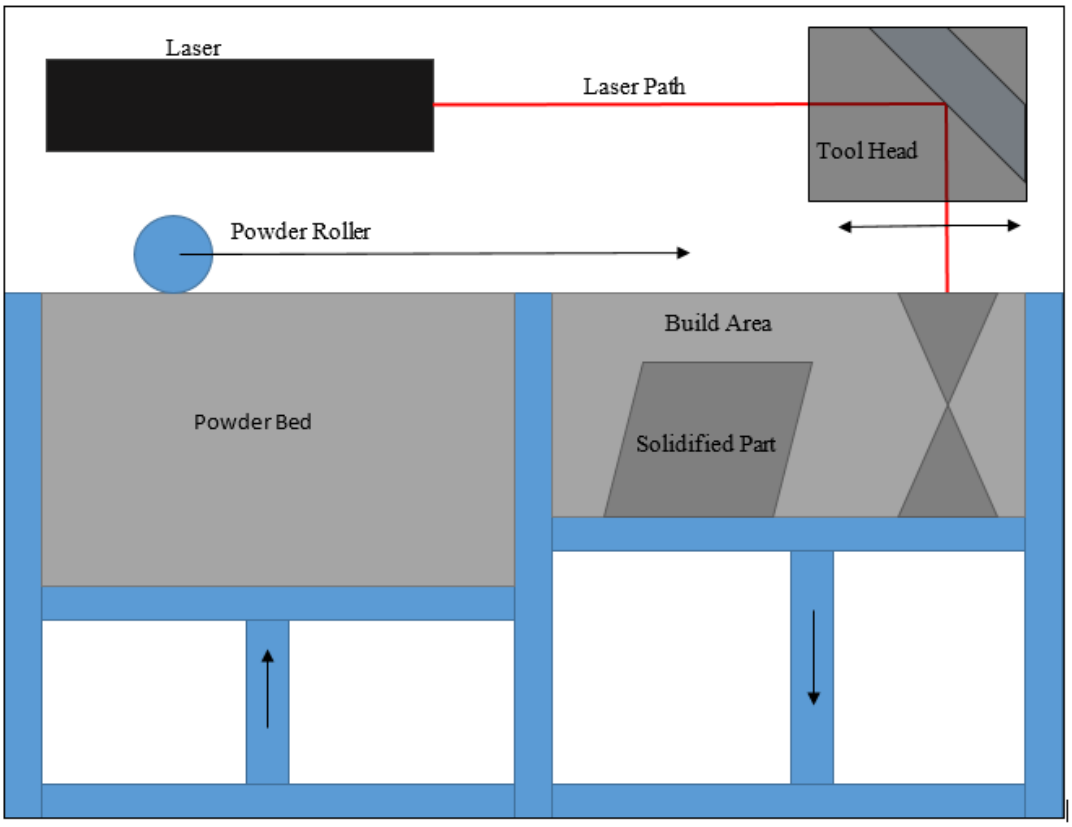

Figure 3: SLM Diagram

Hanzl et al. noted that while laser speed and power were the two largest contributors to the final structure, and thereby the final properties, the angle of the part relative to the build plate is critical in determining the mechanical anisotropy of the part: for example deviations from 45 degrees decrease the tensile strength along the vertical direction. The hatch angle, or the rotation of the laser pattern between layers, can also negatively impact the mechanical anisotropy of a final part. Much like the orientation relative to the build plate's vertical axis, a hatch angle 45 degrees is the ideal [8]. Although processes have been proposed to determine ideal print parameters by determining the response of the material to single tracks, single layers, and demonstration parts [9], this approach was not possible in the current study due to limited material supply as well as limited access to the SLM machines which are operated by Arctos.

2.3.2 ADVANTAGES OF ADDITIVE MANUFACTURING WITH METALS

There are three key advantages AM offers over traditional machining processes for creating finished parts: limited or no tooling investment per part, novel part geometries are possible, and layer-by-layer property control. As this report is focused on investigating the viability of these parts as electric motor components it will only focus on the first aspect: the ease with which one can import and build motor parts of traditional design using ferromagnetic metal powders. The other two advantages provide interesting opportunities for future research: utilizing AM to print novel motor components for increased performance, and optimization of build parameters for AM-printed magnetic materials through layer-by-layer control.

One of the most pronounced advantages of using AM is the low-cost investment in testing new part geometries. Novel designs may be tried with minor adjustments to the powder bed, tool head, and build environment for little to no added cost while more conventional methods such as casting or punching require a large initial investment in creating the dies and tooling. Creating new parts with an AM system is as simple as loading a 3-D model of the desired part, arraying it with any others on a virtual representation of the build plate, selecting the desired

parameters, and pressing start [10]. This is the primary advantage of AM that will be explored in this report due to the desired product comparison. While this advantage has been documented for many years across all material systems and fields of application, little work has been done to date with ferromagnetic materials intended for motor applications. The recently published literature in this area will be discussed in subsequent sections.

The second and most distinct advantage of additive manufacturing is the unique design geometries made possible by a layer-by-layer build approach. This enables additive parts to have complex, high resolution internal structures such as cooling channels that would be impossible to produce through a traditional casting process [11]. Although this is not the focus of the current study, it is an area of great opportunity with certain key limitations that must be overcome first, chiefly the necessity of support stock to hold a build in place during construction. While AM does offer increased flexibility in the geometry of a part along the build height, the high-power laser passes will weaken or sometimes even melt the material in a previously deposited later [11]. This is necessary to ensure the layers are bonded together sufficiently, but it means that some geometries must have additional support structures built to maintain the final shape of the part. While suitable for small test batches, an increase in post machining to remove the supports must be warranted by a substantial increase in the part's performance over traditional machining methods.

The final potential advantage that additive manufacturing offers over traditional methods is the custom control of the composition and properties that appear on a layer-by-layer basis. To alter the composition one can adjust the powder blend added to the work area as the build progresses, making significant alterations to the makeup of a part along the build direction. Additionally, one can vary the properties of a consistent powder feed by changing the build parameters with build height. This change comes in the management of heat along the build surface, with proper care one can change the phase at which the melted material resolidifies. This

is achieved by altering the power of the laser, the speed at which it moves across the part, and the pattern chosen to cover the entire build surface. By locally controlling the cooling rate, one can add internal stresses to counteract planned external stresses on a part or even change the grain structure of the part layer by layer. Depending on the alloy chosen one could build motor components with high resistivity and high polarization layers in a single build, eliminating the need to cut and laminate thin layers [12].

2.3.3 DISADVANTAGES OF ADDITIVE MANUFACTURING WITH METALS

Because additive manufacturing eliminates the cost of tooling, the only potential cost investment that can be recovered through subsequent builds is the discovery of ideal build parameters for novel materials, as there are relatively few materials well studied in an AM environment, such as Ti-6AL-4V [11]. Ultimately additive methods eliminate the need for specialized tooling but have a higher per part cost in materials (due to the high cost of metal powders) and in manufacturing time due to the limited size of build areas. A 2014 survey of the capabilities of AM techniques and their possible applications showed that the largest AM build areas were around 1 square meter for LENS powder feed techniques, and the smallest were 0.1 square meters for SLM powder bed machines [11].

It is possible to decrease the build time of additive parts, but this generally comes at the cost of physical properties. As less total heat is applied to a part (either from lower laser power or higher tool speed) there is less penetration of melted material per layer into previous layers or lack of melting all together, leading to lower density and greater porosity overall [13, 8]. However, it is also possible to overheat and ablate the powder if too much heat is applied. This can lead to similar problems in porosity as the material is ejected from the build surface and there is poor bonding between layers.

In addition to porosity, poor planning of a build whether through build path choices, heat management, or time constraints, can also lead to poorer mechanical performance. These choices can lead to residual stresses inside of the part which can reduce the overall strength of the final part. However, it is known that one can control the buildup of residual stresses normal to the build direction through smaller hatches, controlling the orientation of the hatches relative to the outer wall facing (45 degrees is optimal), and increasing the energy per distance input from the laser (i.e. higher power at lower speeds) [14, 8].

There also exists a certain amount of anisotropy in the AM fabricated parts. This anisotropy can impact the mechanical performance of a part, for example in AM fabricated steel samples the impact strength can be up to 3 times larger in parts built normal to the build plate compared to parallel to the build plate [15]. Similarly, the yield strength and ultimate tensile strength of AM steels exhibited up to a 30% increase for the same parts. However, it was found that the hardness of the final part was not dependent upon the orientation of the build direction [15]. Despite the penetration of melted layers into previously built layers, the z orientation consistently exhibits the worst physical performance in AM parts [11]. Additionally, the orientation of the build may result in magnetic anisotropy as discussed previously under the ferromagnetism section. However, this will not be an area of concern for this report as it is known that a magnetic annealing cycle is required to tune the magnetic properties of the as built Hiperco 50 material system. Potentially it should be possible that the cooling rate of an AM part could be tuned to result in a magnetic structure or for other materials, in which case as-built magnetism could be attained.

Finally, even with the application of procedures that attempt to improve the surface finish of AM processed parts, either from laser finishing passes or secondary clean up lasers, parts built with additive manufacturing still rely on traditional machining methods to remove the stair step effect or unexpected defects before they can be put in use. For the purpose of this study the

surface finish of the part is of small but non-negligible concern, as the rough surface left by the SLM build could contain stress concentrators decreasing mechanical strength and fatigue life even after heat treatment [11]. Even in parts designed to account for the increased stress concentrations, there remains the fact that they must be removed from the build plate (usually via mechanical cutting) and additional support structures must be removed.

2.4 HIPERCO 50

This report focuses on the Carpenter developed alloy Hiperco 50, an iron-cobalt alloy with vanadium, niobium, and carbon added to improve the poor workability of the iron-cobalt system. The specified composition is 48.5% cobalt, 1.9% vanadium, .05% niobium, .01% carbon, and balance iron [6]. For the purposes of this report it will be referred to as a ternary FeCoV alloy as the impacts of the remaining additives are too minute to consider in this report. Additionally, the following sections of this report will discuss the impact of ordering on the final properties of the FeCoV part. It should be noted that the addition of small quantities (under 2.5%) of vanadium into the iron-cobalt system does not impact the order/disorder mechanics to a significant degree [17]. Electrical steel that is currently used widely in electric motor applications is an iron-silicon alloy with up to 6.5% Si added and small amounts (0.5% or less) of manganese and aluminum.

2.4.1 MAGNETIC PROPERTIES OF HIPERCO 50

The iron-cobalt system is known to have extremely favorable magnetic properties, namely high permeability and saturation induction coupled with low coercivity and core loss. There are two configurations of FeCo alloys that favor magnetic or mechanical properties: ordered and disordered. The ordered FeCo system exists as a BCC cubic structure with cobalt replacing iron atoms at the center of the unit cell [18, 19]. This configuration yields the highest saturation magnetization of any known material [20, 21]. This saturation (1950 emu/cm^3- 2.4T) is far greater than either of its primary constituent elements at room temperature (Fe 1710 emu/cm^3,

Co 1440 emu/cm^3) [22, 23 pg 174, 21]. The disordered state on the other hand has no predictable distribution of iron/cobalt atoms, where they may occupy any lattice site in the BCC crystal structure. It is from this arrangement of atoms that the "ordered" and "disordered" names arise. This system is not greatly impacted with the addition of ternary elements into the alloy as Sundar and Deevi noted in their 2005 overview of the iron-cobalt system. For example, vanadium produces the second largest drop in saturation magnetization of all ternary additives, which is only 4.2% [23, pg. 173].

When applied to AC electric motor applications, another key magnetic property of interest becomes the magnitude of core losses of the material. Core losses describe the combination of factors that result in heat losses as the coils align and realign the magnetic fields of the core material. Chief among these are hysteresis losses and eddy current losses, both of which have been discussed previously, as well as anomalous losses which account for the difference in the calculated loss and the observed loss [23, pg. 176]. Generally, Hiperco can be said to offer similar losses to iron-silicon motors of identical geometries, but with the added potential of use in high flux density applications as similar steels are not capable of exceeding 2T [23, pg 176].

Kustas et al. examined the impact of a heat treatment on the magnetic properties of FeCoV alloys when constructed using Laser Engineered Net Shaping (LENS). While LENS is a different approach to AM and the vanadium content of the selected alloy is only 1.5%, it is still valuable to discuss the results when compared to traditional and SLM manufactured parts.

Kustas found that the LENS-produced toroids exhibited a maximum of 4% decrease in saturation magnetization (2.21 T, vs 2.3 T) before annealing and a maximum ~1.7% decrease in saturation magnetization after annealing (2.26T, vs 2.3T) when compared to traditionally manufactured FeCoV. Also, the LENS-produced toroids exhibited a maximum of 1.8% increase in saturation magnetization when compared to pre-annealed, rolled Hiperco 50 (2.24T vs 2.2T)

[24]. Additionally Kustas showed that as built LENS parts showed reduced coercivity to as-rolled parts (995 A/m vs 2900 A/M) but that annealing the LENS parts would not bring their coercivity in line with the annealed rolled product. Kustas only managed to lower the coercivity of one of his specimens to under 400 A/m which placed it within the same order of magnitude but still significantly higher than most literature (90-200 A/m) [24]. Finally, Kustas could not achieve similar relative permeability results to previous literature as well, with his as-built parts averaging at 518, and increasing to 1615 post heat treatment. This falls well short of normal Hiperco permeability given in the literature, which is μ_{max} of at least 4000 with a maximum value of 8000 [24].

Kustas attributes this discrepancy to the finer grain structure of the LENS produced parts as well as unintentional residual stress from the build that was not relieved by the heat treatment. This could very well be possible because while Kustas annealed the parts in the upper range of a magnetic heat treatment (1111K), he only held that temperature for 2 hours but used the slowest cooling rate recommended by the manufacturer to compensate (2.33 K/min or 139K/hour) [24, 16].

2.4.2 STRUCTURAL PROPERTIES OF HIPERCO 50

Hiperco 50 is a ternary iron-cobalt alloy with vanadium added to improve the mechanical performance of the alloy. The data in this section refers to traditionally manufactured (rolled) Hiperco 50 coupons unless otherwise specified. The ductility (and thus the workability) of the material dramatically increased with the addition of vanadium, increasing to 8% elongation before failure in the ordered state (from 0% in FeCo) and to 20% elongation to failure from the disordered state (from 4% in FeCo) [20]. This increase in ductility is attributed to the effect that the added vanadium has in strengthening the grain boundaries in the FeCo system, shifting the primary failure mode of the alloy from intergranular to transgranular [20]. It is known that the ordered FeCo system derives its brittleness primarily from the inability of dislocations to cross-

jump between slip planes, causing these points to become stress concentrations. By introducing vanadium to the FeCo system large scale order is maintained, but localized disordered zones appear as the vanadium atoms tend to form Co_3V precipitates. Additionally, the vanadium addition has been observed to "scavenge" harmful impurities such as oxygen, nitrogen, and sulphur to prevent the formation of compounds detrimental to the structure [25].

The disordered FeCo exhibits a higher yield strength than the highly magnetic ordered state, regardless of post processing steps that alter grain size [26]. This increase is on the order of 100 MPa, more specifically the yield strength increases from 284 MPa for the ordered state to 394 MPa for the disordered state [20, 26]. This yield strength varies with the heat treatment and microstructure of the final product though, with these results being low for a typical magnetic anneal as is intended for use in this report. In its cold-rolled, pre-annealed state Hiperco can exhibit ultimate tensile strengths on the order of 1300-1400 MPa with a yield strength of 1200-1300 MPa [16, 27] although it is highly brittle, with an elongation to failure of only 1-2% [16]. The mechanical favoring anneal cycle reduces this to approximately 800-1000 MPa tensile and 300-400 MPa yield [16, 27], with the lowest strengths of 600-900 MPa tensile and 300-350 MPa yield appearing after a full magnetic annealing [16, 27]. It has been proven that the yield strength is due to the presence of short-range ordering in the normally disordered state [20].

Various novel production methods such as equal channel angular extrusion can increase the tensile strength of fine-grained Hiperco to 900-1400 MPa with a yield strength of 650-700 MPa while exhibiting more ductility than the cold-rolled part [28]. If nanometer scale grains are achieved, Hiperco 50 is capable of yield strengths up to 2.1 GPa with 13% ductility, according to the Hall-Petch relationship where yield strength increases inversely with grain size:

$$\sigma_y = \sigma_i + k_y d^{-½} \tag{6}$$

where σ_i is lattice friction stress and k_y is a constant of grain boundary strengthening.

Paradoxically k_y is higher for the ordered state over the disordered state, meaning that with nanometer scale grains, grain boundary strengthening can become the key driver of yield strength in Hiperco 50 [29].

The order-disorder state of the FeCo system can be controlled after the final machining of the desired part through a selective heat treatment. Carpenter Electrification suggests a heat treatment of 1300-1600 °F for 2-4 hours in a dry hydrogen or vacuum atmosphere, cooling 250-400 °F per hour until 600 °F is reached, then free cooling to room temperature. The higher temperature annealing is recommended to increase magnetic performance at the cost of strength, as the degree of ordering in the post anneal specimen is directly related to the maximum temperature of the heat treatment. The degree of this ordering is not binary; thus a balance can be found between the desired property tradeoff. It should be pointed out that the 1600 ºF upper bound is a hard limitation as any temperatures above this will lead to the formation of an austenite phase that begins to negatively impact magnetic performance [16].

Through their experiments with binary AM iron-cobalt Babuska et al. suggested that it may be possible to entirely suppress the formation of the ordered FeCo state through SLM and its associated higher cooling rates. This is in agreement with Kustas et al who were able to reduce the presence of the ordered phase by effectively increasing the cooling rate of each layer of a part by increasing the head speed of the laser and increasing the time between each layer build [30]. With proper parameter tuning to eliminate unnecessary defects it was proposed that an AM iron-cobalt part could exhibit three times the strength of a conventionally manufactured part and 6 times the ductility [31]. While this report is focused on binary FeCo and the resulting mechanical properties, the implications for such a dramatic increase in performance are noteworthy. Although the goal of the current study is to maximize the magnetic performance of the AM material, it should be noted that in scenarios requiring a balance in properties ultra-fine grain structures, and

multiscale microstructures can be preserved in heat treatments under 600°C [31]. For a summary of Hiperco properties, including all the properties mentioned in the previous two sections, see Table 1.

Table 1: Summary of Hiperco 50 Properties of Interest

Density (g/cm^3)	Yield Strength (MPa)	Ultimate Tensile Strength (MPa)	Elongation to Failure	Saturation (T)	Coercivity (A/m)
8.12	300-500	600-900	1-2	2.3	90-200

CHAPTER 3

EXPERIMENTAL METHODS

3.1 PART BUILD

3.1.1 POWDER SELECTION

The powder used for this experiment was a FeCoB1 blend obtained from Homogeneous Metals Inc. (Clayville, NY). The received composition was disordered (B1) Hiperco 50 with a powder size ranging from 1.01 to 248.78 μm. There were two powder blends considered for this project with different size distributions. A Morphologi 4 automated imaging machine (Malvern Panalytical, Almelo, the Netherlands) was used to determine the size distribution of each of the provided powders (courtesy Mark Benedict, AFRL). The Morphologi 4 took high resolution images of the sample powder, calculated the pixel area of each distinct particle, then generated a circle of equivalent area to the pixelated image and output a distribution of the particles based on this circular equivalent (CE) diameter. The powder batch classified as "#1 -500 mesh" had a lower maximum powder size of 168.12 μm and had two distinct distribution regions with the majority of the powder being under 50 μm in size, this can be seen below in Figure 4.

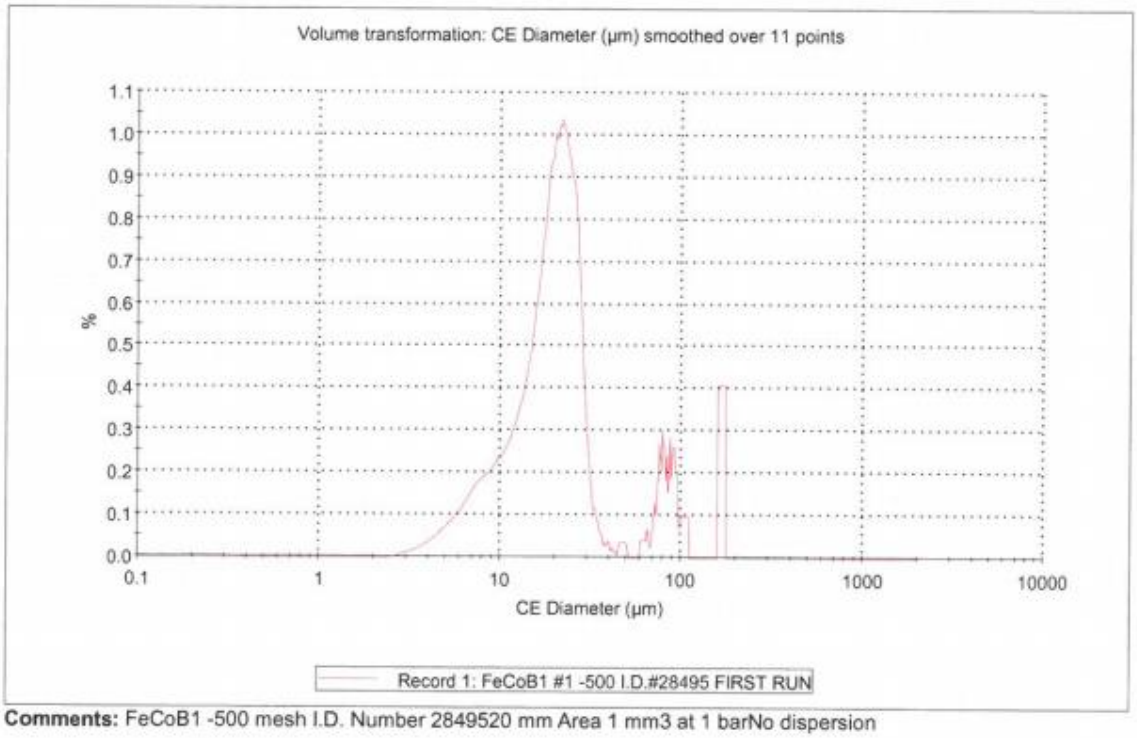

Figure 4: Powder #1 Size Distribution (courtesy Mark Benedict, AFRL-RX)

The second batch of powder that was analyzed was classified as "#5 -20/+500". This batch exhibited the full range of powder size mentioned above yet the vast majority of the powder fell in the 20-200 µm range. This full distribution can be seen below in Figure 5.

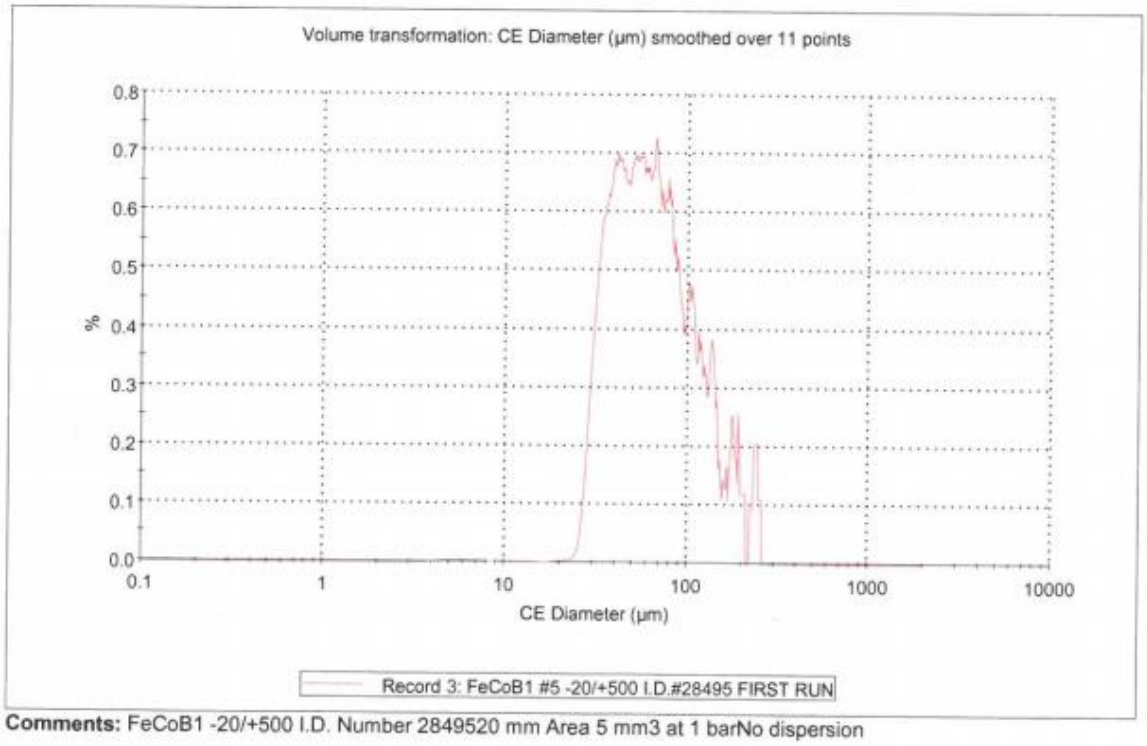

Figure 5: Powder #5 Size Distribution (courtesy Mark Benedict, AFRL-RX)

Based on this analysis and two test builds that will be discussed in the parameter selection section, the team based at Arctos (Fairborn, OH) determined that the second powder (#5 -20/+500) would be better suited to their machine due to a combination of factors. The first deciding factor was that the more even powder distribution would lead to a more uniform and dense powder bed each layer. The second consideration was that the smaller powder, batch #1, would be more sensitive to overheating and possibly ablate away more readily, thus the larger powder was chosen.

3.1.2 3D PRINTER

The printer used for this report was a development test bed produced by Open Additive LLC (Beavercreek, OH). This equipment is commonly used for refining novel material build parameters and control software development. The machine contained an IPG YLR-1000-WC-14 single mode, continuous wave, ytterbium fiber laser, operating at a wavelength of 1070 nm and power of up to 1000W. While this laser is more powerful than lasers in typical commercial additive manufacturing equipment, the full extent of this range was not required in this study and can be replicated with lower power lasers. The laser beam was focused by a F-theta lens from Ronar and had a focal distance of 255 mm and a spot size of 40 μm. The build occurred in a closed 30 inches x 40 inches x 30inches chamber purged continuously with argon to prevent oxidation. This system also gathered visual and thermal tomography data at the start and finish of each build layer for post-build analysis, although this information was not used in this study.

3.1.3 BUILD PARAMETERS

This thesis project grew out of a government-industrial collaboration between AFRL and Arctos. Near the beginning of thesis work, the build parameters were selected by the Arctos group using the following approach. Initially small-scale proof of concept structures were built to select the better powder lot from the two available. These structures, referred to as “test grids”, were comprised of a series of small 1 cm x 1 cm squares printed directly on a flat steel plate. Each square was printed with a different combination of machine parameters, demonstrating the effect of laser power, laser speed, and hatch spacing on the final build quality. This first round of powder viability testing was conducted on a smaller powder bed to conserve material. These grids consisted of a 5x5 array of squares, with laser power parametrically increasing by 60 W increments from 100 to 340 W, and laser speed by 150 mm/s increments from 500 mm/s to 1100 mm/s. The default hatch spacing of these builds was 70 μm, and the powder layer depth was set at 30 μm. The qualities of these builds were primarily rated on their surface finish and appearance as

it is a good indicator of the degree of melting, and if any ablation occurred which was indicated by a smooth, wavy surface finish with the laser final laser path leaving a clearly visible depression along the surface. It was determined at this point to continue only with powder #5 -20/+500: not only was it the powder available in the greatest quantity, but also even the best test squares from powder #1 exhibited noticeable surface porosity.

Once the powder viability builds were completed it was deemed necessary to move to the machine with the larger print bed to have enough vertical build height to accommodate vertical tensile specimens. To confirm that the new machine configuration would produce similar results to the smaller test bed, a new power-speed test grid was printed for the same parameters as described above. During this build there was a problem with a suspected large plastic contaminant in the powder, so this grid was removed from consideration. The powder was then sieved with an 80 mesh (177μm) unit and returned to Arctos for re-evaluation. Because the original powder contained very few FeCoB1 particles of this diameter, it was not retested for particle size distribution.

With the sieved powder and the larger test bed machine, two test grids were printed for best parameter selection by Arctos. The first of these grids was a 5x5 power-speed grid as before (powers ranging from 100 W to 340 W in 60 W increments and speeds of 500 mm/s to 1100 mm/s in 150 mm/s increments, layer depth was still set at 30 μm) except the hatch spacing was set to 90 μm rather than 70 μm. For the second set of grid, based on prior experience with this machine the laser was set to -2 mm from its ideal focal length, which increased the spot size from 45 μm to 100 μm. This practice had led to better final parts in other builds previously completed by Arctos across material types. The comparison between parts made with focused and unfocused laser beams will be made later in this report. Upon completion of the first test grid, Arctos determined via visual inspection that squares made with the 280 W power setting were the best in surface finish and maintaining final build geometry, thus this power was selected for

further investigation of the parameter of hatch spacing. An additional test grid was produced having hatch spacings ranging from 70 μm to 150 μm in 20 μm increments and laser speeds from 800 mm/s to 1400 mm/s in 150 mm/s increments, while the layer depth was still maintained at 30 μm and laser beam unfocused. Again, through visual inspection, it was determined that the 70 μm hatch spacing was best, and combined analysis between these two showed that the best acceptable speed was 950 mm/s.

3.1.4 SPECIMEN MACHINING

Using the final parameters from above, Arctos built two identical assemblies of parts, one with the laser in focus and one with the laser out of focus (positioned -2 mm from its focal length, changing the spot size from 45 μm to 100 μm). These final assemblies or "plates" contained a 3-inch tall neumotors stator pattern to be sliced into 0.007 inch strips for lamination in a final motor, a 3-inch tall toroid stack to be sliced into ¼ inch tall toroids with an outer diameter of 1-½ inch and an inner diameter of 1-inch, eight 3-inch tall tensile bar stock (4 horizontal and 4 vertical configurations), and ten 1.5-cm tall by 1-cm x 1-cm density cube stock (selected for ease of density calculation). The final configuration can be seen below in Figure 6.

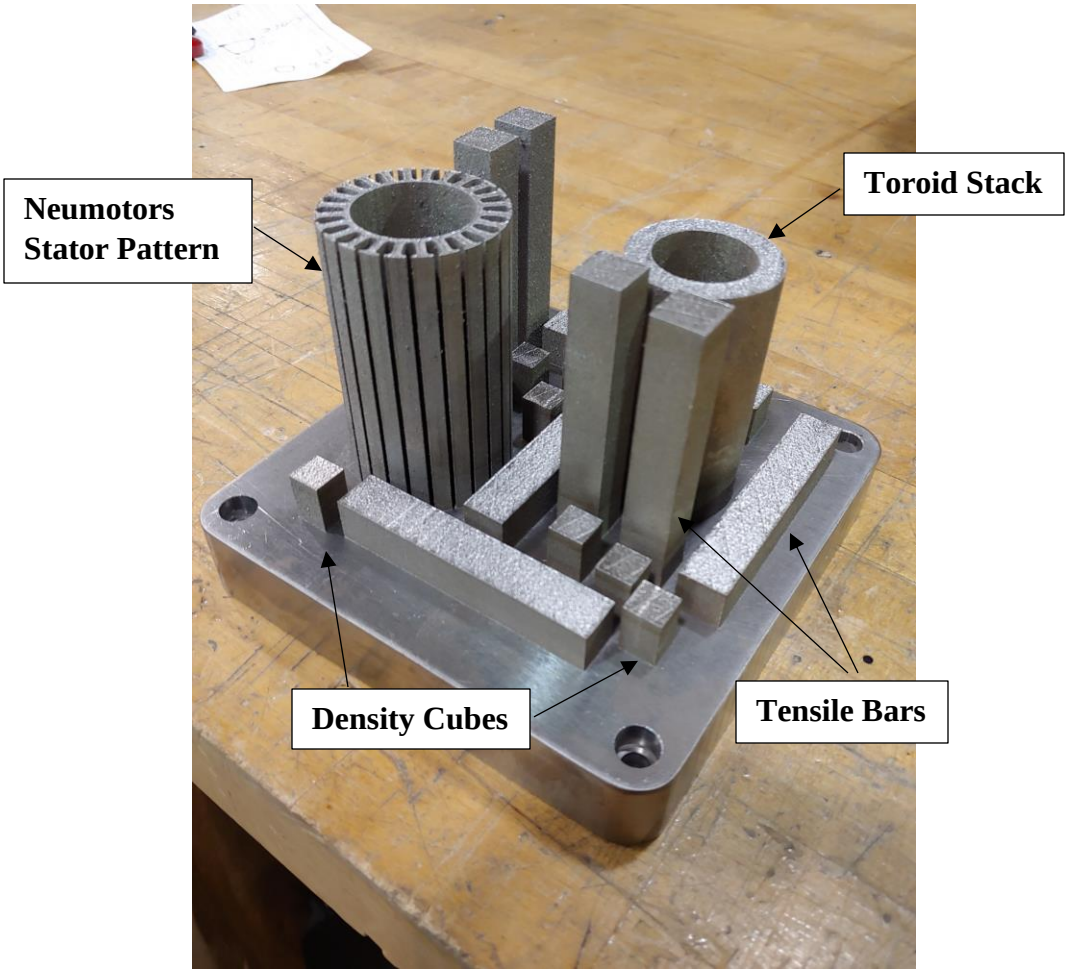

Figure 6: Final Build Plate with assembly of parts

During the final build process it was observed that the quality of the finish of the focused beam build plate dropped approximately half-way up the build height. This change was noted to coincide with the clogging of an air quality sensor. A surface level inspection of these parts shows a change in the surface roughness and coloration of the final parts.

Next, the two plates were taken to an AccuteX Sp-500i Electric Discharge Machine (wire EDM) to separate the parts from the base plate. A wire EDM utilizes electrical discharges between the charged tool-electrode (wire) and the workpiece-electrode (part), which cause a dielectric breakdown in a stream of water directed at the cut line. This results in the removal of workpiece material, which is then flushed out of the resulting gap by a continuous stream of

pressurized water from the top tool head. This method was chosen as it allowed for a clean cut surface without significant heat buildup that may alter the microstructure of the final part or induce unnecessary stresses. An image of this process may be seen below in Figure 7.

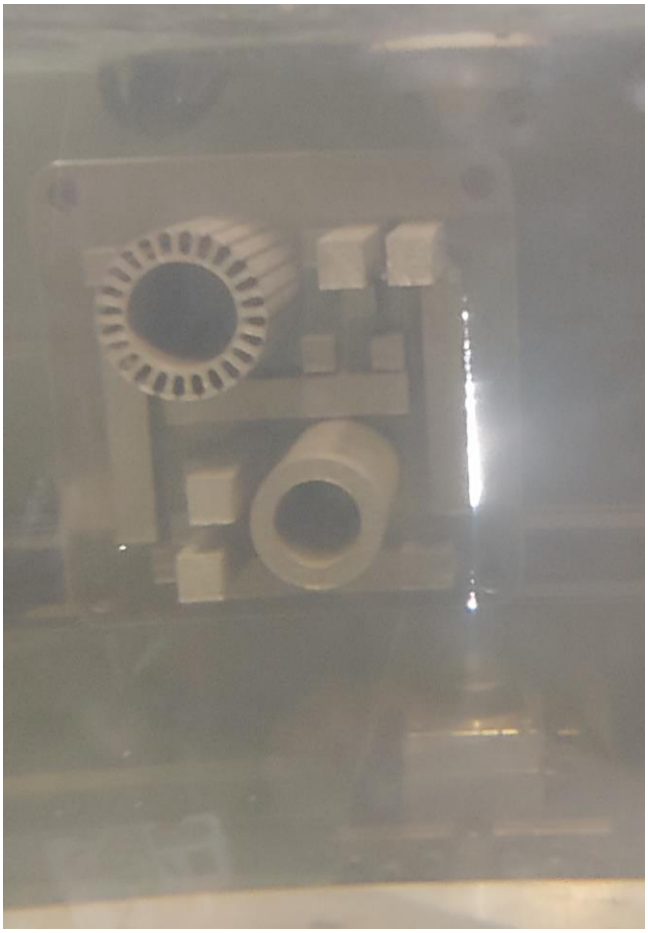

Figure 7: Build Plate Orientation in Wire EDM Tank

After all parts were removed from the build plate, the density cubes and tensile specimens were taken to the University of Dayton Research Institute (UDRI) machine shop for the next stage of preparation. The density cubes were milled down to 1 cm cubes, removing the excess vertical height in the build and roughly cleaning excess material from the bottom plate mount surface. The tensile specimens were prepared to a standard previously used by the Air Force Research Laboratory (AFRL), seen below in Figure 8, except that in place of a specimen

number a dot was placed on the top end of the vertical specimens and on the top of the end of the horizontal specimens (similar to the specimen number placement as shown below). This allowed the distinction of the highest point in the build, so that any defects could be correlated with the position on the build.

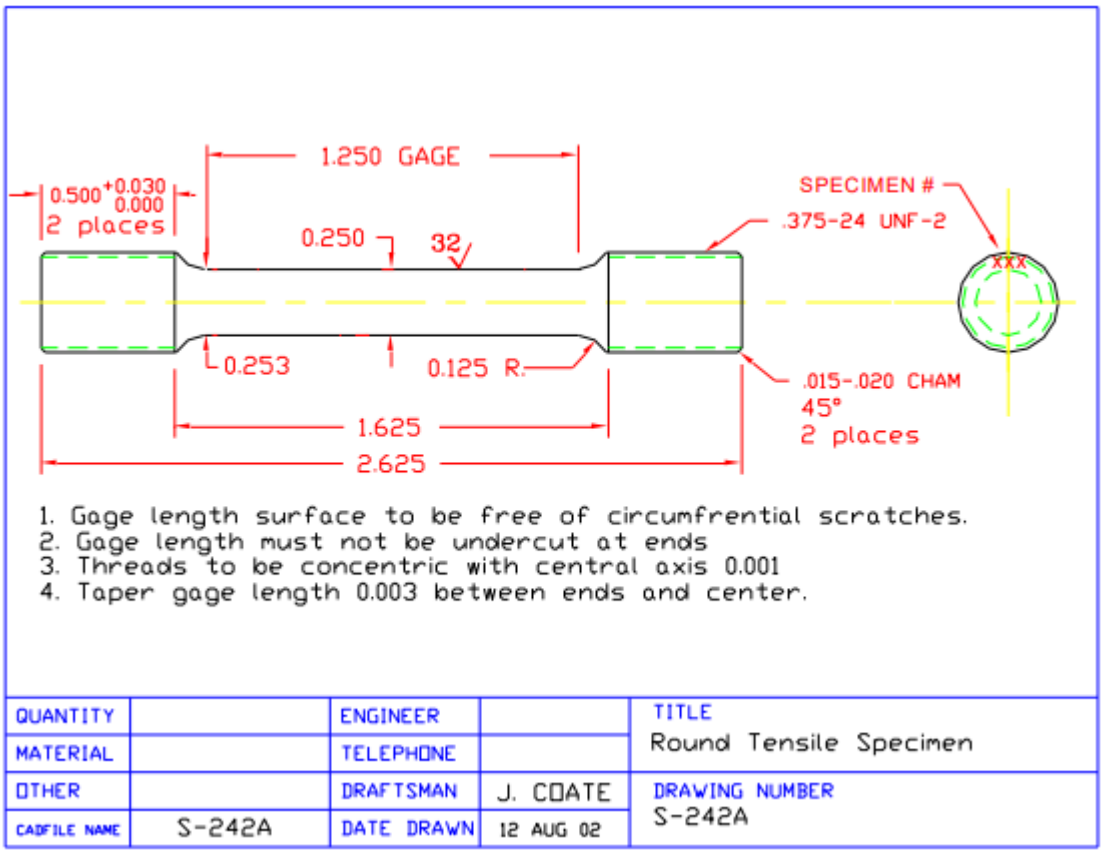

Figure 8: Tensile Specimen Drawing, all units given in inches

While the density cubes and tensile bars were sent to a professional machine shop for fabrication, the creation of the toroid specimens and stator laminations was performed at AFRL using the same wire EDM that was used to remove the parts from the build plate initially. The cylindrical specimen used to make the toroids was gripped directly by the adjustable part grips and oriented out into the cutting area. After each toroid was separated from the cylinder, the

cutting process was stopped, and the part was immediately dunked in an oil bath and then dried to minimize oxidation from the deionized water from the wire EDM tank. The starting cylinder was 3 inches in height, and 6 toroid specimens at ¼ inch in height were desired. Therefore, the loss of machinable material due to the grip orientation was acceptable.

3.1.5 HEAT TREATMENT

As discussed in the literature search, most Hiperco parts intended for magnetic purposes must undergo a magnetic annealing cycle in order to optimize their microstructure and increase their magnetic properties. Half of all of the machined parts (cubes, tensile bars, and toroids) were taken to Winston Heat Treating in Dayton for a magnetic anneal of 1570 °F (±25°F) for 4 hours, cooling at a rate of 400 °F per hour until 600 °F was reached, then free-cooling to room temperature. This annealing was done under vacuum, and the parts were placed in individual baskets so a comparison could be made between pre and post-heat treated states by tracking which sample was which.

3.2 PROPERTY TESTING

3.2.1 DENSITY MEASUREMENT

Several independent methods were used to assess the density of the printed cube samples. To begin with, the mass of each of the cubes was measured using an Ohaus Explorer scale with 0.01 g precision. The cubes were placed into individual sample bags to distinguish them without marring the surface and handled with gloves to prevent any contamination that may impact the final mass. Thus, the first density calculation was taken as simply the recorded mass divided by the sample volume ($1cm^3$), meaning that the measured mass could be used as a rough estimate for density. This measurement is generally not ideal: while it does account for the porosity of the entire specimen, it also assumes that the cubes are entirely square and exactly to specification. This simple calculation was used as a baseline to ensure the other results are reasonable.

To get a more accurate measure of the density of these cubes, the exact volume must be recorded. To this end, a Micrometrics AccuPyc II 1340 gas pycnometer (Micrometrics Instruments Corp., Norcross GA) was used. This device used helium displacement to measure the volume of a specimen. The test involved filling the test chamber with helium with no standards inside, sealing off the chamber entirely, then a valve opened to a secondary balloon which was inflated to measure the amount of gas from the filled chamber. This chamber was then calibrated with two solid spherical standards with a combined volume of 12.741508 cm^3. During testing the chamber was filled and evacuated by the balloon a total of 10 times, which was then averaged by the control software. To speed the testing process for the cubes, one of these standards was left inside the test chamber, reducing the total volume of helium pumped in and out during each testing cycle. The standard sphere's volume was then subtracted from the total displayed value to give the volume of each cube. This method allows for a high degree of penetration of helium into the pores of the material, thus it was not a measure of the cube's bulk density, but of the actual consolidated metal materials. However, it is not likely that the helium penetrated very far down due to the overall low levels of porosity, therefore it was considered to be an approximation of the bulk density, potentially giving artificially high densities due to pore penetration.

To confirm the density measurements a third method was employed using liquid water, intended to account for the surface roughness of the cubes while not penetrating deeply into the interior pore. A Mettler Toledo Excellence scale (0.0001 g precision) was used to perform a density measurement according to ASTM D792 [32]. This test is based on the Archimedes method which uses water displacement to measure the density of an object. The cubes were first individually weighed above the basket and water bath (weight in air, m_{cube}), and then completely submerged inside the bath and weighed again (weight in water, m_{water}). The difference in the masses was used to calculate the density of the cubes according to Equation 7 below. During testing this was done automatically by the scale, but confirmed afterward using the masses

recorded during each step of the process. This is a simplified relationship, as the volume of the fluid displaced and the volume of the cube are equal since the cube is fully submerged, meaning a direct relationship can be established between the densities and masses of the cube and displaced water. Additionally, the mass of the displaced water can be derived from the difference in the mass of the dry and submerged cube.

Figure 9: Equipment used for ASTM D790 density measurement: (left) scale with buoyancy fixture, (right) close up of submerged cube being measured for its weight in water

$$m_{cube}/\rho_{cube} = m_{water}/\rho_{water} \quad (7)$$

3.2.2 MICROSTRUCTURE ANALYSIS

Once the density testing of the cubes was completed, they were then prepared for evaluation at a microstructural level. To begin, the cubes were first sectioned such that the interior of the specimen could be evaluated both parallel and perpendicular to the build direction. This was accomplished with the Accutex wire EDM, where 5 cubes at a time were gripped with wide jawed vice grips (Airtech International), and the vice grips were extended into the cutting

area, this can be seen in Figure 9 below. These 5 cubes were oriented vertically, such that one cut from the vertical wire would split all of the cubes down the middle, exposing the interior Z-plane. In the below figure the wire would span from the top to bottom of the image, and then advance from left to right, into the jaws of the vice grips, splitting all 5 density cubes in half. To keep track of which halves came from which cube, the top and bottom of each cube was numbered with a welding pencil that was found to not wash off while submerged in the EDM. These cubes were immediately removed from the bath, submerged in oil, and then dried to prevent oxidation as with previous EDM cuts.

Figure 10: Density Cube Cutting Grip

Once the cubes were sectioned for interior inspection, they were prepared for mounting and polishing. Labels were printed identifying each sample by its number, focused/unfocused beam condition, as-built/annealed state, and the x-y/z orientation. Samples were grouped together by cube number and both orientations of every cube number were placed in their own mount. Buehler sample cups (1.25 in. diameter) were treated twice with a coating of mold release to ease sample removal.The samples were placed face down on the bottom, and the corresponding labels were placed on the outside edge, facing outward such that the sample identity could be clearly determined from the side of the specimen. The epoxy potting compound was comprised of EPON 862 and Jeffamine D-230 amine curing agent at weight fractions of 74.1% /25.9% respectively. This system was selected for its optical clarity for ease of reading the internal labels. Approximately 15 g of resin was prepared for each cup by mixing manually in a paper cup and pouring into each of the mold cups. Any large air bubbles in the epoxy were popped with a wooden stick, and finally the samples and labels were adjusted into their final position with toothpicks until left to cure overnight. Each sample was removed from its mold the next day.

Next the grinding and polishing process began. The grinding was carried out by hand using a Buehler Handimet roll grinder with running water, beginning with 240 grit paper until the sample surface was filled with scratches in a single orientation. Next the sample was rinsed and manually ground with 320 grit paper until the previous scratches were removed. This manual process continued to 400 grit and 600 grit paper before an automatic rotary polishing wheel was used (Buehler Automet Ecomet model 250). The polishing wheel began with 800 grit paper and running water, using a single force holder, and counter-rotating the head and paper. An initial force of 2 N (per sample) was increased by 1 N every 30s until 4 N was reached, and then this condition was maintained for a total of 3 minutes. This process was repeated for 1200 grit paper, and as well as the final polish. The final polish was done with a 0.05 μm alumina suspension on a lapping cloth for 3 minutes. After this final polish the samples were rinsed under water and

washed with Ivory soap and cotton swabs to remove the last of the polishing media. After dabbing dry with Tec Wipes, they were considered ready for optical microscopy.

Once the final polish was completed the samples were taken to a Zeiss optical microscope in the AFRL Materials and Manufacturing Directorate to build a complete image of the surface porosity before etching. The microscope included an automated surface stitching feature, where it moved and refocused the image according to a predetermined grid path defined by the user. This produced 200-300 images per sample which were automatically stitched together to form one composite image to be evaluated in ImageJ software to determine the percentage of porosity in these sections, as well as to show the relative size of the pores in each sample and sample orientation. In ImageJ the image was first cropped to remove the specimen edges, scale bar, and any large surface defects from the polishing process that would impact the porosity data (large scratches, water spots, etc.). Then the image was converted to a black and white image by making the image 8-bit, then black and white from the toolbar. From this cleaned black and white image, the pores were measured by running the "analyze particles" function, which numbers, outlines, and records the area of every pore on the surface. In this case edge pores were omitted to better measure the absolute size of the pores, and the tabulated results were output including a size summary.

To examine the crystalline microstructure and composition of the cube specimens two different methods were attempted. The first was a chemical etch, wherein two different etchants were applied. This first attempted etch was a 15% nitol solution, this was applied for 110 seconds before being rinsed off with water, then alcohol, then air dried to remove water spots. The second etch was an anhydrous Kallings solution, applied for 15 seconds, then cleaned identically to the nitol etchant solution.

The second method used to identify the microstructure of the samples was using the compositional backscatter mode of a JEOL JSM-6060 SEM and JSM-IT500HR SEM at AFRL.

Due to the non-conductive nature of the potting epoxy, charging from the beam would become an issue if the samples were directly placed into the microscope. Therefore, they were first placed in a vacuum chamber overnight to remove any lingering moisture in the epoxy, then sputter coated with a Denton Vacuum DV-502A RF sputter system to add a 50 Å layer of gold atoms over the surface to improve conductivity. This was run with a base pressure of $3x10^{-6}$ Torr, with a working pressure of 6 mTorr, a flow rate of 55 sccm argon, and a forward power of 100 W. Then to further improve the conductivity a strip of copper tape was run from each sample around the side of the epoxy to make direct contact with the screws holding the samples in the sample holder. This precaution was taken due to the high beam voltages necessary for examining magnetic specimens as well as the non-conductive nature of the epoxy.

Once these backscatter images were collected, they were saved and exported to ImageJ much like the porosity data. However, these images were analyzed manually, using the built-in measuring tools to record the size of individual grains by highlighting their total area.

3.2.3 TENSILE TESTING

The tensile specimens were tested at AFRL Materials and Manufacturing Directorate according to ASTM E8. These specimens were placed in an MTS tensile testing machine with threaded grips (.375 inches x 24). A clip-on extensometer was placed at the center of the gauge section of each specimen. Before the testing began the specimens were pulled to approximately 200 MPa (or until the plotted load-deflection curve started to exhibit nonlinear behavior) to ensure that they were seated properly in the grips and that there was no movement of the specimens in the threads. This process was repeated until there was minimal hysteresis of the loading and unloading curve during this test.

Once the specimens were seated and ready for testing, a constant stroke-controlled load was applied at a rate of 5 mm/minute until failure. The Young's Modulus, 0.2% offset yield

strength, ultimate tensile strength (UTS), and strain at UTS were all calculated from the resulting stress/strain data set. The modulus was found by selecting the largest linear region possible of the tensile test data, then applying the excel "best fit" linear line function to the region, which also gives the R^2 error value to represent the quality of the line fit. This calculation was confirmed by calculating the slope via the difference in stress and strain from the minimum and maximum points of the targeted region.

3.2.4 MAGNETIC TESTING

Once the magnetic toroid samples were cut from the build cylinder their preparation for testing could begin. The toroids were first weighed on the same scale that initially weighed the density cube specimens. Then they were wound with ¼ inch wide polytetrafluoroethylene (PTFE) tape to insulate the core and keep the edges from breaking the insulation on the outside of the winding wire, which would cause electrical shorts. Next the secondary coil (N2) with 50 winds was wrapped around the core with 28 gauge magnet wire in a counterclockwise direction. This wire was transferred to the core from the coil via a plastic shuttle. An image of this winding process can be seen below in Figure 10. The secondary coil was then wrapped with another layer of PTFE tape to insulate it from the primary winding, and the ends of this coil were also marked with PTFE tape to separate them from the primary coil. Finally, the primary coil (N1) was wound, starting from the point where the secondary coil ended, and 250 windings were made for the primary loop in the same counterclockwise direction. When the primary coil began to overlap itself along the length of the toroid, the bottom layer of windings was insulated again with PTFE tape to reduce risk of shorting and for ease of winding. The ends of all of the coil wires were stripped of their protective enamel coating using 80 grit sandpaper. Then the positive and negative leads were identified such that power entered the loop via a lead on top of the toroid and exited it counterclockwise on the bottom of the toroid.

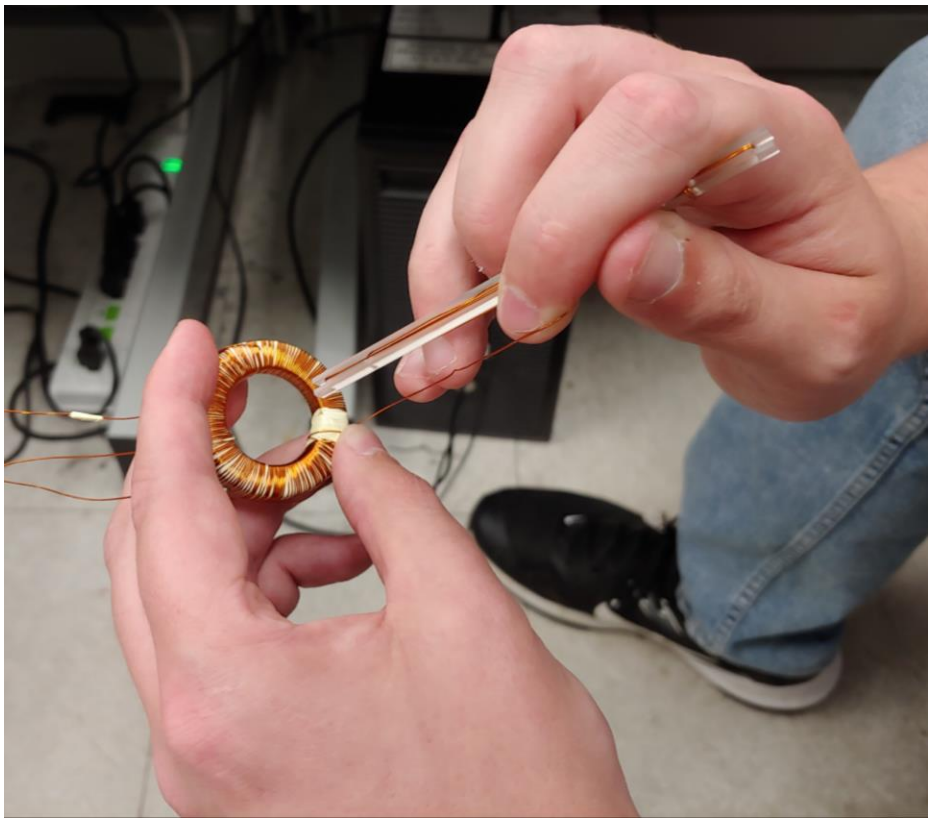

Figure 11: Coil Winding Process

Once the cores were wound the magnetic testing could begin. The cores were connected to a Remagraph-Remacomp Combination hysteresisgraph (Magnet-Physik, Cologne, Germany), which applied a current through the primary winding and recorded the response in the secondary winding generating a B-H curve during hysteresis testing. The hysteresisgraph program requires the inputs of core mass, number of primary and secondary windings, interior and exterior diameter, as well as the height of the core. The program automatically calculated the path length, which is the measure of the circumference of the center of the windings (in this case is 1.5708 inches). Prior to the hysteresis measurement, the magnetometer first ran a demagnetization process to ensure that the sample rings started with no residual magnetization. For each sample the magnetometer was run 5 times, where the first 3 applied a maximum H of 100 Oe to the primary coil, the 4th applied 150 Oe, and the 5th 200 Oe. This increase in applied H was intended

to show that the previously recorded measurements were of a completely saturated core, and that the displayed B-H curve was not of a minor loop. A core was observed as having achieved saturation when increasing the applied field no longer increased the length of the B-H curve along the H axis.

After initial as-cut magnetization data was recorded, a selection of the best performing cores were unwound and had the PTFE tape removed. Next the edges or the edges and surface were sanded to reduce the risk of sharp edges and rough surfaces breaking the magnet wire enamel causing shorts. These samples, indicated as “S” (for sanded edges and surfaces) and “SE” (for sanded edges), were then rewound via the same process and before and retested. All of the magnetic samples data was compared against a forged Hiperco specimen previously run on the same magnetometer prepared in the same manner described above.

CHAPTER 4

RESULTS AND DISCUSSION

4.1 DENSITY MEASUREMENTS

The mass of the density cubes can be seen below in Table 2, As-Built refers to the specimens selected for no further alterations, Pre-Anneal refers to the 10 specimens (5 of each group) selected for annealing before the cycle was completed (to measure any changes in mass and density caused by the treatment), and Annealed refers to these specimens after treatment. Note that the As-Built cubes were held from heat treatment for future microstructural analysis. The As-Built and Pre-Anneal specimens showed some variation stemming from the deviation in samples on the build plate and final machining. Of note here is the clear discrepancy between results for the cubes printed with focused and unfocused beams. Barring a consistent difference in specimen size, it is apparent from this stage that the *focused* beam parts are less dense than their *unfocused* beam counterparts. Also of note is that there was a slight (~0.02%) mass loss in the annealed specimens.

Table 2: Density Cube Mass Results (all masses in units of grams)

	Focused			Unfocused		
Specimen	As-Built	Pre-Anneal	Annealed	As-Built	Pre-Anneal	Annealed
1	7.7080	7.6392	7.6246	8.0313	8.0698	8.0684
2	7.6574	7.7886	7.7819	8.0055	8.0365	8.0358
3	7.7586	7.6691	7.6565	8.0066	8.1187	8.1187
4	7.6824	7.7208	7.7110	8.0565	8.0087	8.0074
5	7.7127	7.7295	7.7188	7.9398	7.9732	7.9715
Average	7.7038	7.7094	7.6986	8.0079	8.0414	8.0404

As stated in the experimental section, these mass values can also be used as a rough estimate for density calculations since the cubes were ideally 1 cm^3. The expected density of Hiperco 50 is 8.11 g/cm^3, meaning that either these cubes were undersized or there was considerable porosity in the cubes. This distinction can be made easier using the next two methods.

Using the pycnometer, a much more accurate measure of the density was found, by dividing the mass seen above in Table 2 by the volume of each specimen as found by the 10 point average of the pycnometer. The volumetric data can be found in the appendix as Table 1a. The volumes of all cubes were slightly lower than the expected 1 cm^3, with the cubes produced with an unfocused beam being slightly larger (~0.988 cm^3) than the cube produced with a focused beam (~0.975 cm^3). It is also interesting to note the relative volume change between pre-annealed and annealed samples: the value *decreased* for focused laser samples while it *increased* for unfocused laser samples. The resulting calculated density of the cubes can be seen below in Table 3. These densities are observed to be much higher than in Table 2, as the volume of the cubes never exactly achieved the 1 cm^3 of the specification. This is troubling though, as it suggests the as-built unfocused specimens exhibit a density slightly higher than what is possible for Hiperco 50, for example a density of 8.1235 g/cm^3 when compared to the standard density of 8.11 g/cm^3 for the cold-rolled form. This issue will be further evaluated with the porosity measurement results, as small pores would allow the helium gas to penetrate into subsurface pores artificially decreasing the volume measurement and increasing the apparent density.

Table 3: Density Results Calculated from Pyconometer Volume and Measured Weight (all density units given in units of g/cm^3)

	Focused			Unfocused		
Specimen	As-Built	Pre-Anneal	Annealed	As-Built	Pre-Anneal	Annealed
1	7.8990	7.9112	8.0156	8.1254	8.1224	8.0990
2	7.9391	7.9014	7.9405	8.1140	8.1471	8.0923
3	7.9362	7.9273	8.0079	8.1209	8.1348	8.0986
4	7.9019	7.8918	7.9723	8.1090	8.1074	8.0922
5	7.9192	7.9194	7.9639	8.0983	8.1060	8.0902
Average	7.9191	7.9102	7.9800	8.1135	8.1235	8.0945

Additionally, this data set shows that in all 5 of the focused beam density cubes, there was an increase in density after annealing, while there was a decrease in density for the unfocused beam cubes. This is a direct result of the volume results which followed the opposite trend. In contrast, the density decreased during annealing for *both* focused and unfocused beam cubes when measured with ASTM D792 as discussed next.

ASTM D792 (density via water buoyancy) was used to help reduce the potential impact of the permeability of the porous sample. The results, given in Table 4, were in between the two previous methods as expected, as it accounts for the true volume of the specimen unlike the mass calculation when $V=1cm^3$ was assumed, and the water does not penetrate and displace the air trapped inside of the cubes to the degree that the helium does. These results show a consistent trend of density loss after heat treatment and densities below the expected 8.11 g/cm^3.

Table 4: Density Data From ASTM D792 (all density values given in units of g/cm^3)

	Focused			Unfocused		
Specimen	As-Built	Pre-Anneal	Annealed	As-Built	Pre-Anneal	Annealed
1	7.7060	7.6390	7.5650	8.0560	8.1010	8.0260
2	7.6930	7.7680	7.7140	8.0090	8.0930	8.0250
3	7.7640	7.6480	7.5900	8.1060	8.1070	8.0660
4	7.6580	7.7000	7.7050	8.0850	8.1010	8.0270
5	7.7190	7.7560	7.7170	8.0890	8.0880	7.9940
Average	7.7080	7.7022	7.6582	8.0690	8.0980	8.0276

From these results it can be shown that increasing the spot size of the laser by unfocusing the beam consistently improved the density of the final part, resulting in final densities roughly 99% of the expected value. Focused beam builds consistently exhibited densities of approximately 95% of the ideal value given the results of this test. It is concluded that ASTM-D792 gave the most accurate results, and the material produced with a focused beam is expected to have more porosity than that produced with an unfocused beam.

4.2 MICROSTRUCTURAL ANALYSIS

The first analysis conducted into the microstructure of the AM Hiperco parts was the analysis of the porosity. Figure 12 shows an example of an optical micrograph obtained from one of the density cubes via the Zeiss optical microscope prior to any post processing. These images were used to illustrate and measure porosity. The porosity of the samples was visually apparent without the aid of a microscope in the case of the focused specimens (both as-built and heat treated), and while this was the case for some of the unfocused specimens there was generally a smaller concentration of voids. This issue will be discussed more at the end of this section along with the average size of these pores.

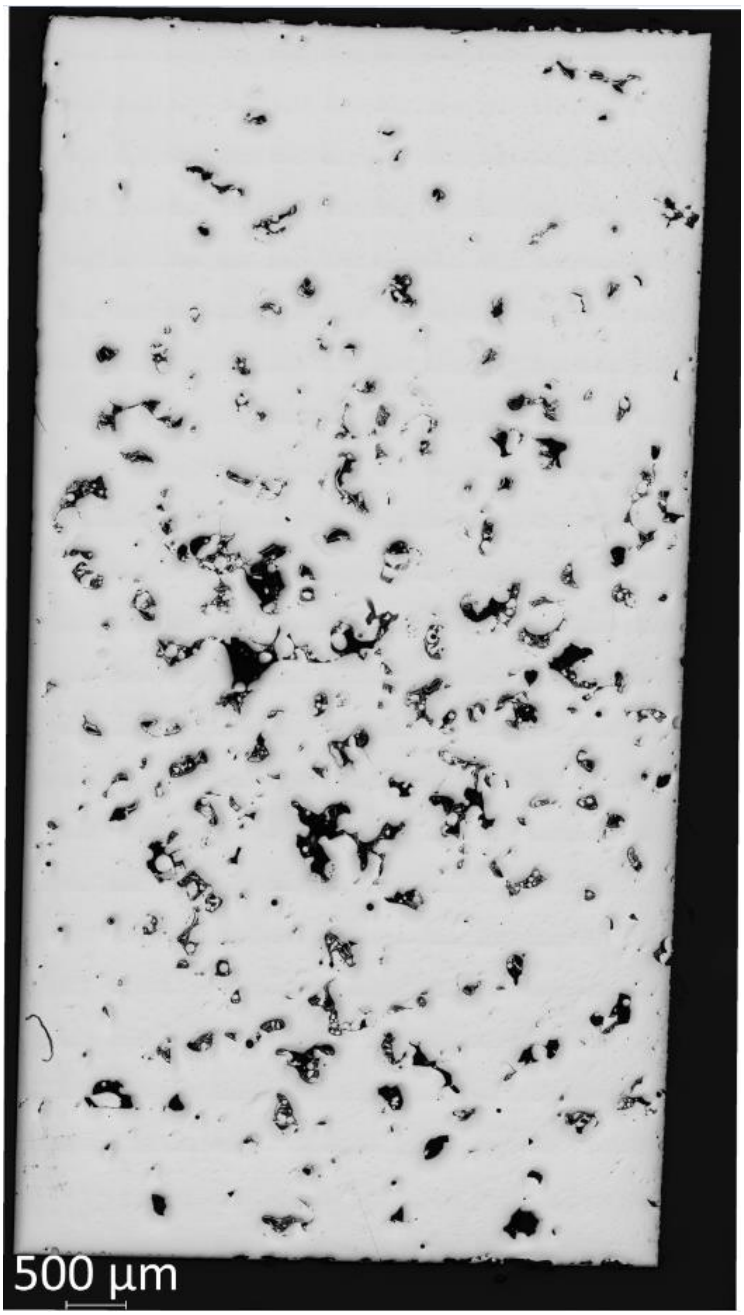

Figure 12: Optical Micrograph of Focused Beam Specimen 2, X-Y Plane (F-2 XY)

Once surface images were taken for all specimens, they were cropped to remove the surface roughness and any marred regions that showed scratches or water spotting. The cropped images were then processed in ImageJ in the manner described in Chapter 3; a final processed porosity image can be seen below in Figure 13. This image processing converted all surface irregularities to black (255) and the surface to white (0). This process was repeated for all density cube parameters in all orientations, for a total of 20 final images, composed of anywhere between 100 to 300 composite images depending on surface area.

Figure 13: Black and White Porosity Map of Specimen F-2XY

In this image the individual pores are numbered and measured by the program, which allows for a calculation of average pore size and size distribution. The pore size results averaged across all five cubes for each of the four material and process variables (focused or unfocused beam, as-build or heat treated specimen) is shown in Table 5, and the size distributions can be seen in Figures 14 through 17. The data is averaged across images taken from XY and Z planes (note that after final machining only the Z direction could be determined, thus Z images could be XZ or YZ. Anisotropy in these planes is not known to occur through the SLM process and as such is disregarded), after minimal anisotropy was observed. From this data it is evident that the largest impact on the porosity are the build parameters, with the focused beam specimens showing much larger and more numerous pores than the unfocused beam specimens. The porosity results are reasonably consistent with the density results, which indicated the focused beam samples were about 95% dense and the unfocused beam samples greater than 99% dense.

It is difficult to establish the direct impact of the heat treatment process on the porosity of the specimens, as there was a large deviation in porosity within each group, but it appears that heat treatment had no strong bearing on the final porosity of the part. The focused heat-treated specimens best exemplified the random nature of the porosity in the slices, with visible porosity ranging from 2-10% of the total surface area (average of 4.9%), though the focused as-built specimens show porosity from 0.5-6% as well. The complete data set can be found in Appendix A.

Table 5: Average Pore Size Data

Beam Status	Processing	# of Pores	Average Pore Area (μm^2)	% Porosity
Focused	As-built	5284	189.2	2.55
	Annealed	8788	453.7	4.87
Unfocused	As-built	4689	17.4	0.173
	Annealed	3276	28.7	0.197

While this data shows the net effect of porosity on the final parts, it fails to capture the complete picture of the nature of the porosity. The imageJ porosity measurement not only records the number and total area of pores, but also the area of each number assigned pore. Using this data, a series of histograms were constructed to show the nature of the porosity in the final parts, and Figures 14 through 17 show this distribution in the unfocused heat treated specimens.

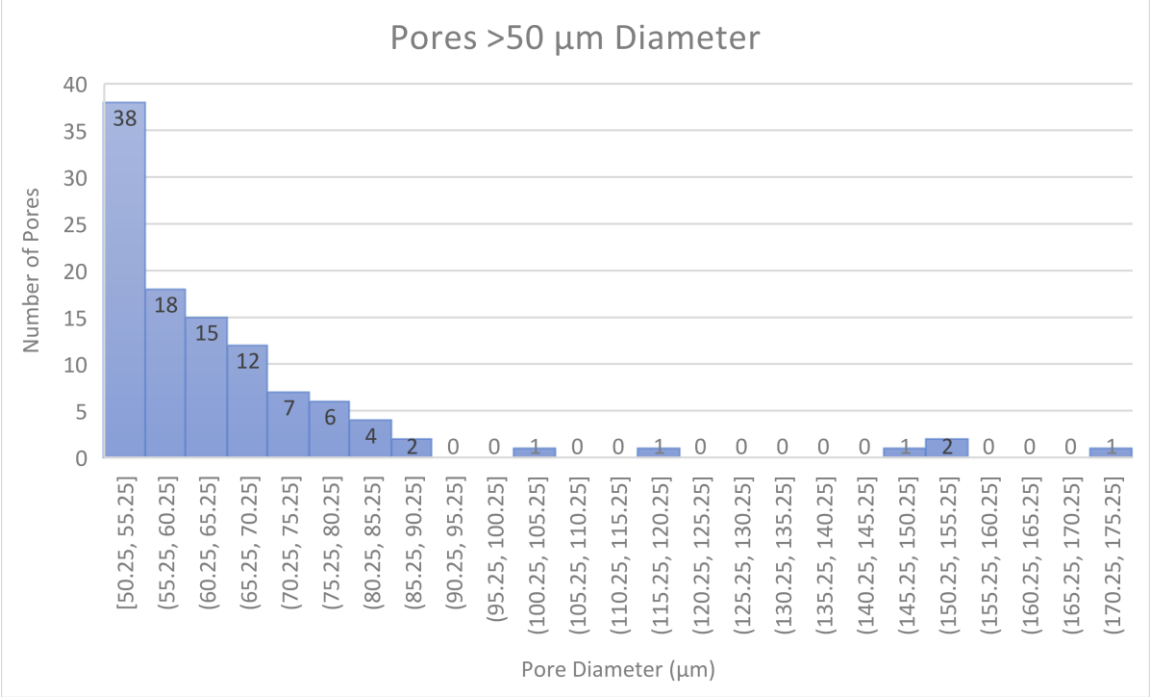

Figure 14: Unfocused, heat-treated specimen Pores >50 um Diameter

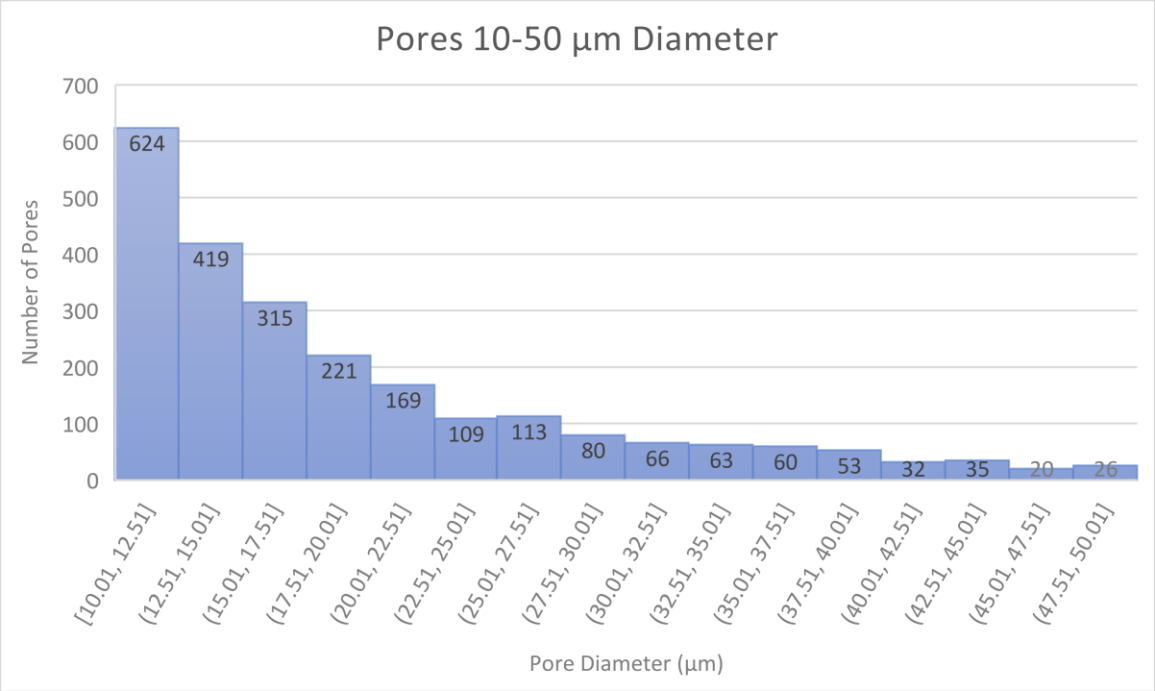

Figure 15: Unfocused, heat-treated specimen Pores between 10 and 50 um Diameter

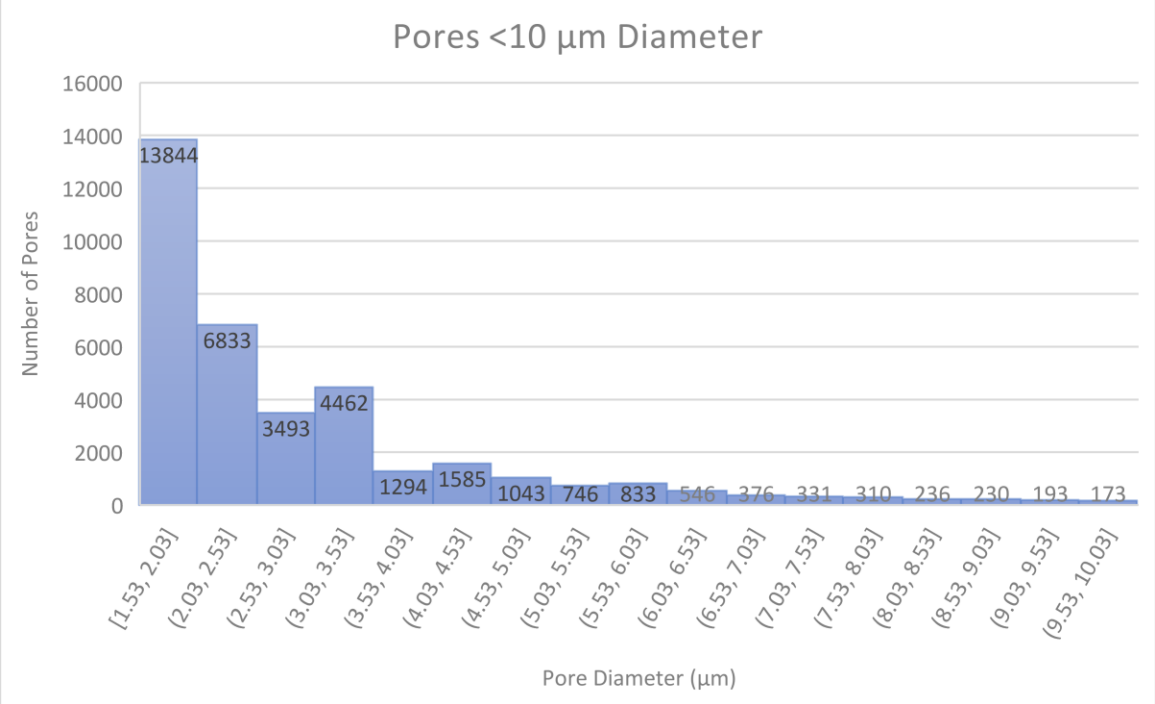

Figure 16: Unfocused, heat-treated specimen Pores Below 10 um Diameter

These histograms show that while there are several large pores with diameters greater than 100 um, less than 100 total (Figure 14), there are over 18000 pores between 2-5 um and over 13000 instances of pores smaller than 2 μm (Figure 16).

While the porosity was easily observable with an optical microscope, additional effort was needed to visualize the grain structure. Hiperco 50 was found to be resistant to the etching required to make the grain structure observable under the optical microscope. The attempted nitol and Kalling's etchants did little to show any underlying grain structure, though the nitol solution enhanced the visibility of the melt pools. As an alternative, a scanning electron microscope was used in compositional backscatter mode. The grain structure then became visible as regions with different coloration. The figure below shows the resulting backscatter image from the as-built state. After heat treatment the grain structure appeared much clearer and easier to measure, nd will be observed later in Figure 19.

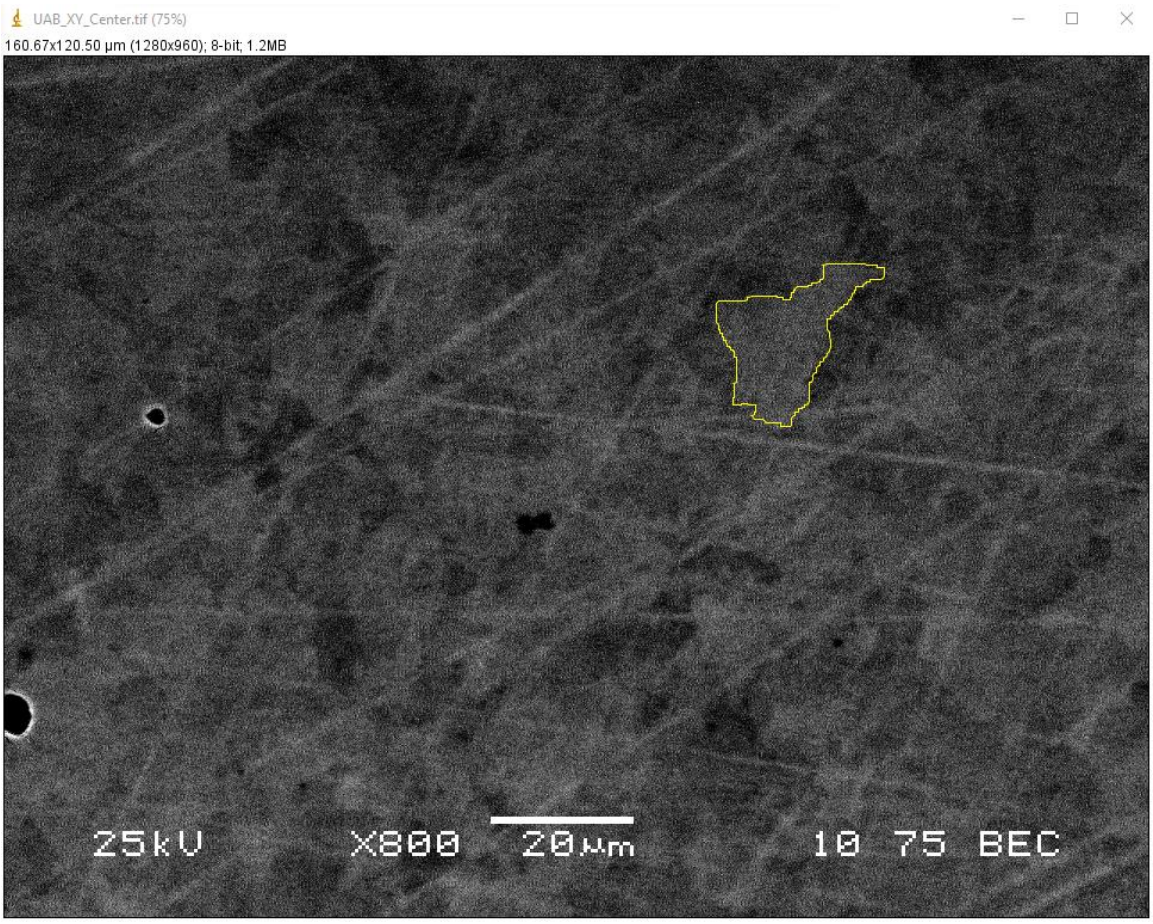

Figure 17: Sample Grain Outlining and Measurement in ImageJ for unfocused beam, as-built specimen

The most clear and well defined grains were manually outlined and measured in ImageJ, which gives the total enclosed area of each grain in square micrometers. For ease of comparison, the diameter of these grains was calculated treating each grain as circular. It should be noted that the as-built state has some highly irregular grain shapes, one of which is highlighted for measurement in Figure 17 for measurement. There was a wide range of grain sizes observed in both pre-heat treatment and post, but these grains all remained inside the 5-25 micron diameter CE range. From the total data given in Table 6, there was little anisotropy observed in the size of the grains when observed in the XY plane or along the Z axis, indicating that these grains are roughly equiaxial.

Table 6: Grain Size Measurements for all Specimens

Beam Status	Processing	Plane	Grain	Area (μm^2)	CE Diameter (μm)
Focused	As-built	XY	1	143.6	13.5
			2	72.9	9.6
		Z	1	162.5	14.4
			2	10.9	3.7
			3	42.5	7.6
	Annealed	XY	1	365.7	21.6
			2	49.8	7.9
			3	28.1	5.9
		Z	1	210.9	16.4
			2	51.1	8.1
			3	75.1	9.8
Unfocused	As-built	XY	1	254.6	18.0
			2	73.6	9.7
			3	73.9	9.7
		Z	1	56.4	8.5
			2	41.6	7.3
			3	120.4	12.4
	Annealed	XY	1	24.2	5.6
			2	67.5	9.3
			3	21.2	5.2
		Z	1	45.6	7.6
			2	125.9	12.7
			3	97.7	11.2

The heat-treated images also revealed white regions consistently appearing along the grain boundaries of these new, better defined grains (due to the heat treatment). These regions were investigated at a higher magnification and then analyzed using the EDS detector. When measured these particles appeared to be in the right size category to be leftover polishing media from the final polish stage (0.05 micron), but with EDS analysis these regions had a higher than expected concentration of niobium (Nb). At this point the grain centers were readily apparent and found not to have any niobium peaks of note. Therefore, the heat treatment process seems to be a

deciding factor in migrating the trace amounts of Nb to the grain boundary regions. An example of these niobium concentrations can be seen in Figure 18 with Figures 19 and 20 showing the composition of both the precipitates and the grain cores respectively. Similar precipitates of Vanadium have been observed after significant aging at elevated temperature (200 hours at 450 °C), and the presence of these precipitates is noted to increase with aging time [33], though the rapid formation of niobium precipitates after a short annealing cycle is to date unknown.

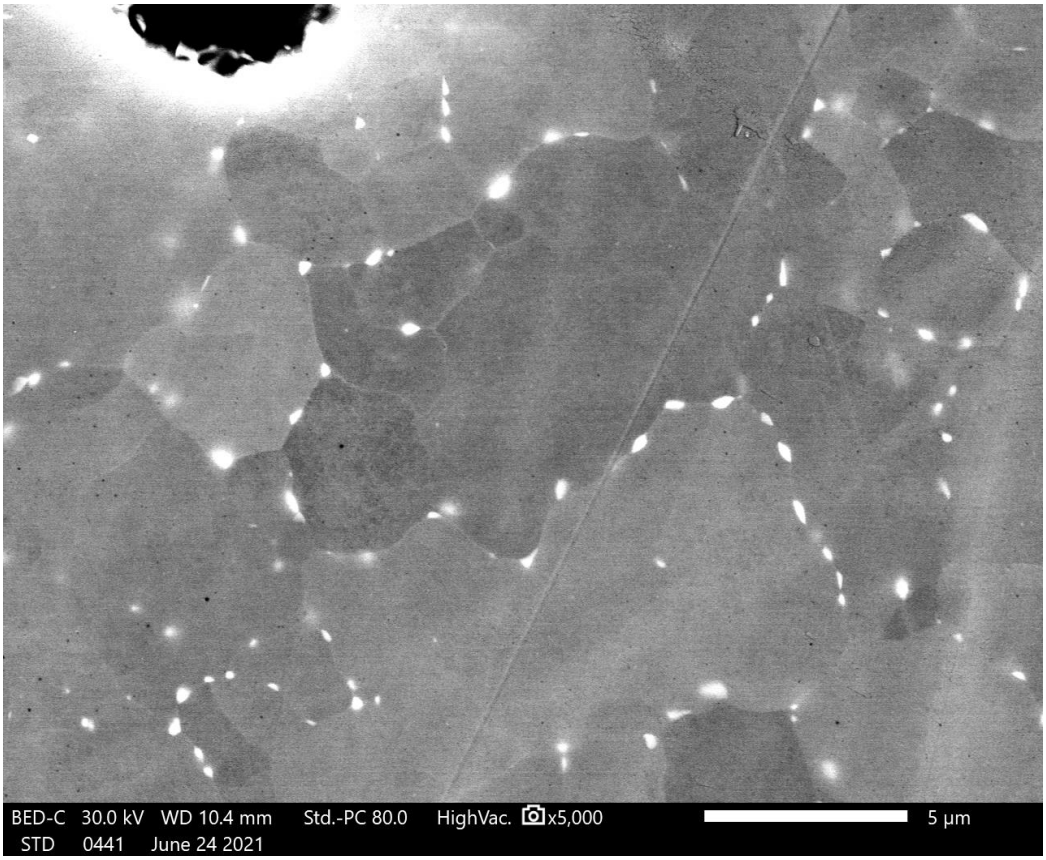

Figure 18: Closer Inspection of Precipitates on Grain Boundaries of Unfocused Heat-Treated Specimen 4

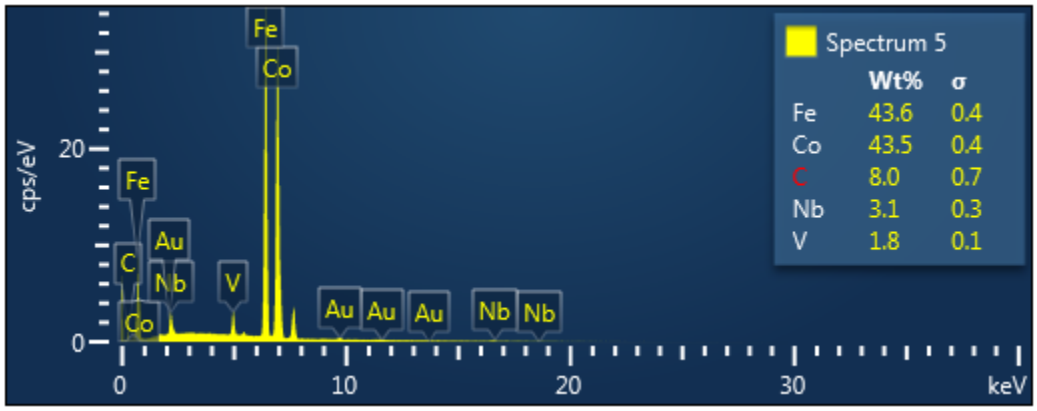

Figure 19: Precipitate EDS Counts

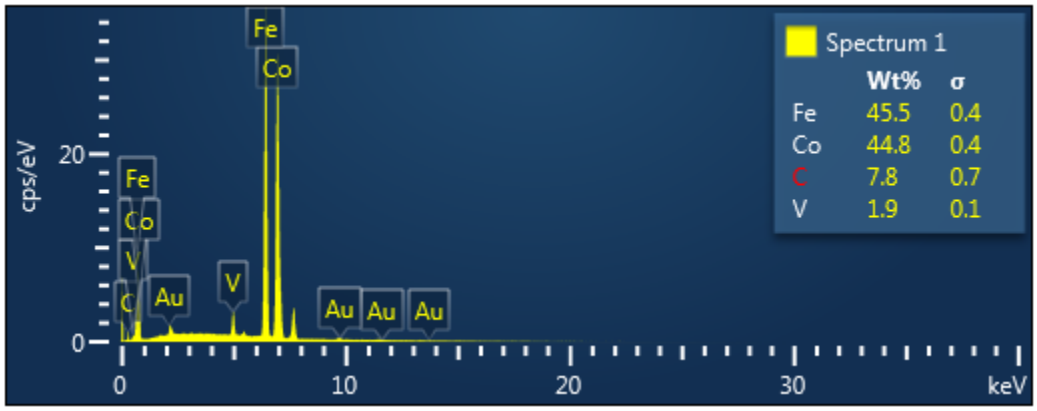

Figure 20: Grain EDS Counts

4.3 TENSILE RESULTS

The tensile results show not only differences in performance based on beam focus and heat treatment status, but also with the build direction of the final part. The as-built specimens exhibited superior properties than traditionally processed Hiperco after conventional magnetic or mechanical annealing. However, there was significant cracking during the heat treatment process of AM-processed specimens that drastically reduced most of the tensile properties, with some samples failing along the cracks in the transition radius outside of the gage region, or some failing before a 0.2% offset yield strength could be established. Figure 21 shows some of the cracking visible in the upper radius of a tensile bar, with Figure 22 showing where failure occurred after the test was initiated.

Figure 21: Visible Cracking in the Transition Radius of unfocused beam, heat treated specimen

Figure 22: Specimen Failed in Transition Radius

Representative stress-strain plots are given in Figures 23 and 24, while the numerical results are compiled in Table 7. For horizontal specimens (Figure 23), the curves progressively changed from high strength and high ductility to increasingly lower values as the beam changed from unfocused to focused, and the specimen condition changed from as-built to heat treated. Also note that ultimate properties (ultimate strength, and strain at UTS) were taken from the point of highest stress as indicated in the figure. Therefore, for the highly ductile samples, the strain at UTS was a small to severe underestimation of the total strain at failure and therefore ductility of the sample. The stress-strain plots for the vertical specimens (Figure 24) were similar to the horizontal results only for unfocused beam, as-built specimens. All the others exhibited a brittle

stress-strain curve and lower ultimate properties. The modulus values of these curves is another issue that will be discussed next.

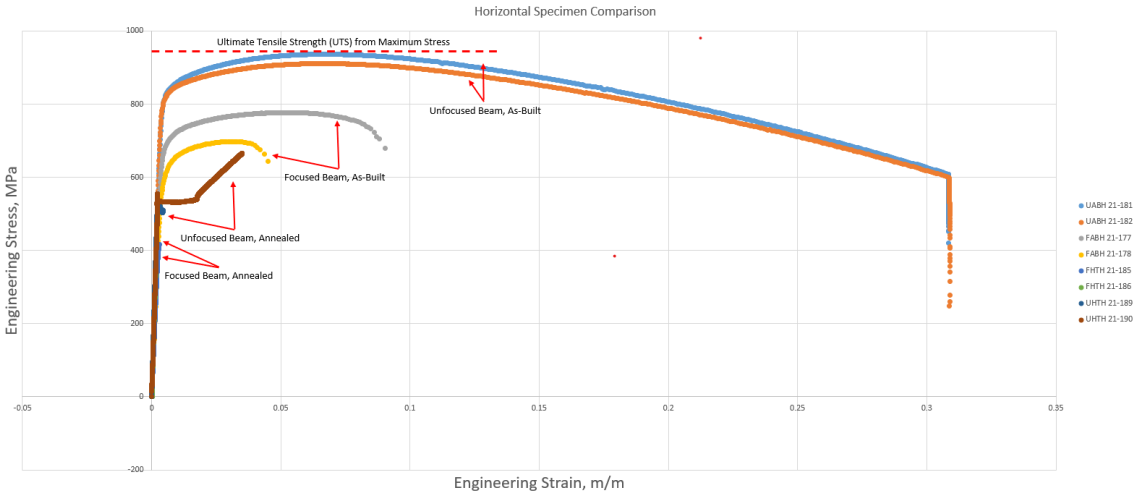

Figure 23: Horizontal Specimen Stress-Strain Plot

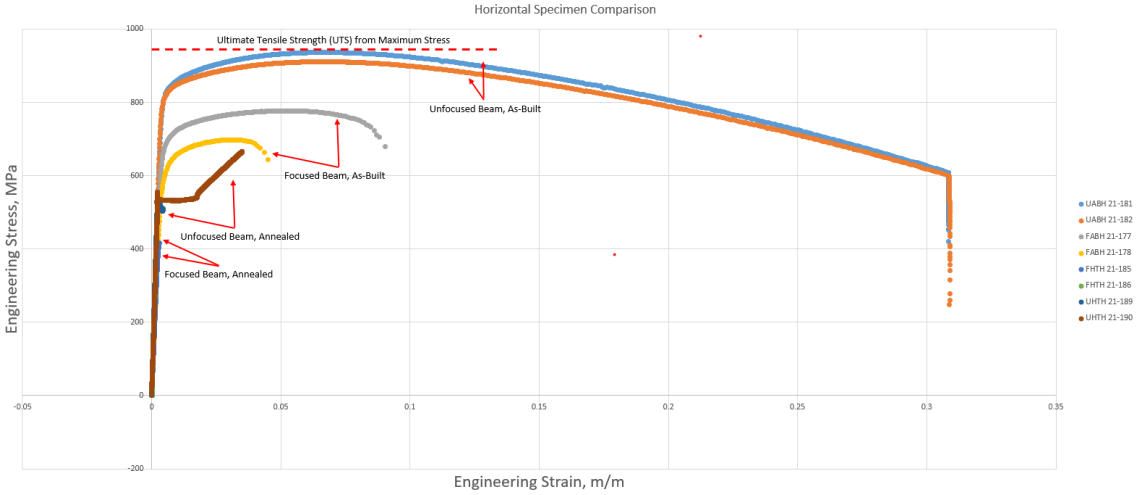

Figure 24: Vertical Specimen Stress-Strain Plot

Table 7: Tensile Results Summary

Beam Status	Processing	Build Direction	Modulus (GPa)	Modulus Fit Region (MPa)	Good-ness of Fit	0.2% Offset Yield Strength (MPa)	UTS (MPa)	Strain at UTS (m/m)
Focused	As-built	Vertical	109	50-200	0.9999	303	309	0.00534
		Horizontal	186	50-400	0.9999	691	777	0.05360
			165	50-400	0.9999	618	698	0.03190
	Anneal	Vertical	103	30-95	0.9946	104x	104	0.00104
			94	40-60	0.9995	108x	108	0.00163
		Horizontal	169	100-300	0.9999	417	417	0.00291
			219	150-300	0.9998	$360x_L$	360	0.00167
Unfocused	As-built	Vertical	204	50-400	0.9991	817	928	0.06330
			215	50-400	0.9999	807	937	0.06320
		Horizontal	215	50-400	0.9999	831	937	0.06460
			206	50-400	0.9999	822	912	0.06240
	Anneal	Vertical	221	150-350	0.9999	$503x^U$	503	0.00225
			241	50-200	0.9928	$410x^U$	410	0.00179
		Horizontal	248	100-300	0.9997	509	530	0.00249
			228	100-300	0.9968	533	665	0.03500
Standard: Rolled Hiperco, Magnetic/Mechanical Anneal			206.8			331/414	792/930	.05/.15

x- 0.2% Fit Could Not Be Achieved

^{U}- Specimen Broke in Upper Transition Radius

$_L$- Specimen Broke in Lower Transition Radius

The first property to be discussed is the modulus of elasticity of the material. This is established by plotting the stress applied by the load frame against the strain from the extensometer, then determining the slope of the line near the beginning of the test when the curve is most linear – this is when the material is behaving elastically and not near plastic deformation. The focus of the beam had the largest impact on this value, with most of the unfocused beam results exceeding the cold rolled values. Even for one unfocused beam vertical build specimen, which broke along a crack in the upper transition radius rather than the gage, there was still an improvement in the modulus. Heat treatment resulted in a trend of increased modulus for the unfocused beam samples. Conversely, the focused beam parts exhibited a significantly lower modulus than cold rolled values. Heat treatment improved the modulus of the horizontal specimens but reduced it in the vertical specimen, and all but one of these specimens yielded and failed before a 0.2% offset yield strength could be established. It is difficult to draw conclusions on the continuation of this trend into larger applications due to the small sample size, but it remains an interesting point in this data. The low strength reduced the number of data points available for evaluating the modulus. A range of 50-400 MPa could be used for the as-built specimens, but this was reduced to as little as 40-60 MPa for the heat treated vertical specimens as given in the "Modulus Fit Region" column. Despite this, the quality of the modulus fit line (extrapolated from an excel best fit line R^2 value) remains high, with over 99% confidence in all cases, though this could be impacted by the small size of the data set on the heat-treated specimens.

The yield strength of all the *as-built* specimens were significantly higher than the rolled parts that underwent a magnetic anneal, except for the vertical orientation of the focused beam parts; however this may be a result of difficulties experienced in the build process rather than characteristic of the build parameters. When compared to the mechanical annealing the differences between the focused and unfocused beam become more prominent. All unfocused

beam specimens still exceeded the yield strength of the mechanical anneal, while only the focused horizontal specimens exceeded it. Again, this may be due to difficulties during this specific build rather than a reflection on the quality of the build parameters, with the print error occurring at a high enough point to only affect the vertical specimens.

The ultimate tensile strength of most of the AM-printed specimens were inferior to rolled Hiperco 50. Only the unfocused beam as-built specimens performed the same or better than the annealed rolled standard (where they were on par with the mechanical annealed rolled standard and significantly better than the magnetic annealed rolled standard). The focused beam vertical specimens exhibited by far the worst performance, failing at as little as 104-108 MPa. Many of the failures of heat treated specimens occurred before a 0.2% offset yield strength could be established, and one vertical focused beam specimen was broken during the machining process, indicating an extremely low UTS.

The maximum strain at failure tells a similar story to the ultimate tensile strength, in that the only specimens to perform better than the low end of the rolled standard range were the unfocused beam as-built specimens. For the rolled standard material across both heat treatment types, a range of 5-15% strain elongation is listed, while the unfocused beam as-built bars elongated to just over 6% before failing. Again, no AM-printed specimens could match the maximum specification of 15% listed for rolled material.

Representative of the differences in mechanical performance seen through the data here, the unfocused as-built samples also exhibited a different failure mode. While the majority of the samples were extremely brittle (some even failing before a 0.2% offset yield strength could be established), the unfocused as-built samples failed in a reasonably ductile manner. These specimens underwent significant necking, down to approximately 50% of their initial diameter, in both the vertical and horizontal orientations. Some examples of the differences in failure modes can be seen below in Figures 25 and 26.

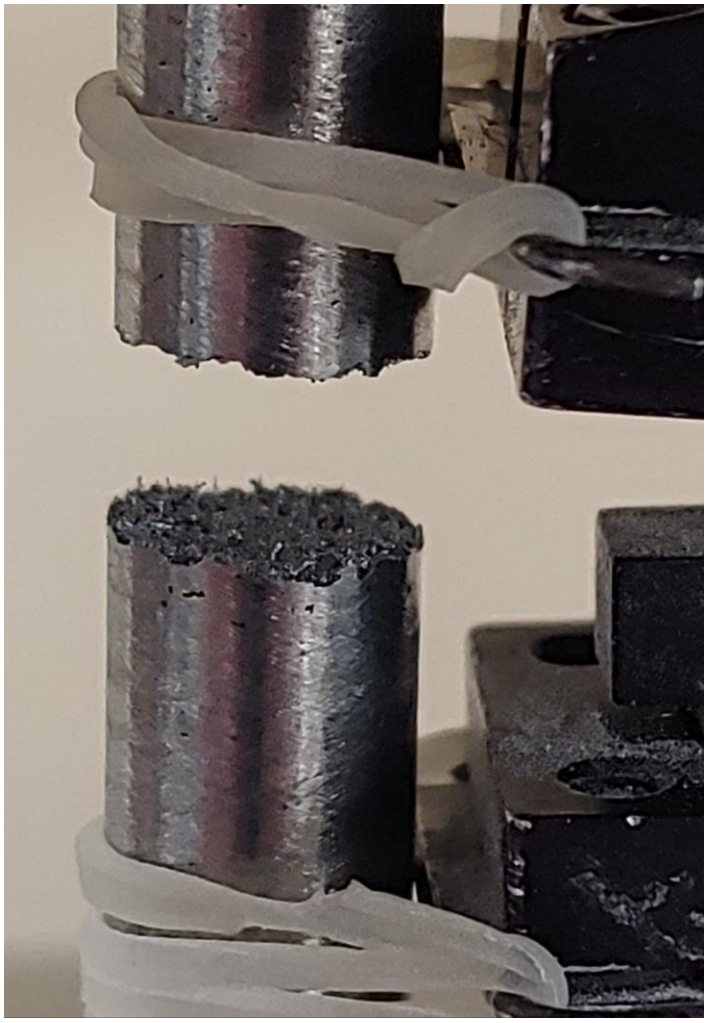

Figure 25: Focused Beam As-Built Brittle Failure

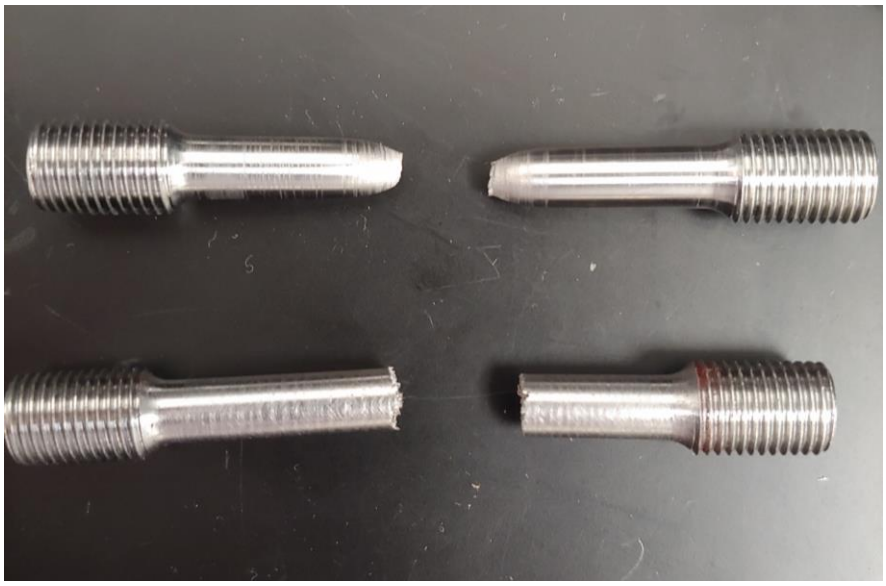

Figure 26: Ductile and Brittle Failure Modes in Unfocused Beam (Top) and Focused Beam (Bottom) As-Built Tensile Bars, Respectively

A summary of the tensile results is given as follows. There is significant anisotropy in the *ultimate properties* of focused beam specimens (horizontal better than vertical), but the unfocused beam samples were more isotropic. Interestingly, the effect of *heat treatment* was to lower the ultimate properties of both focused and unfocused samples, while it had no significant effect on the modulus of either.

4.4 MAGNETIC PROPERTIES

The final and most important step in rating the quality of AM-processed Hiperco for use in electric motors was their magnetic performance. The magnetic performance was primarily graded on their coercivity (Hc) and remanence (Br), which indicate the input field necessary to magnetize/demagnetize a core and the output field when the input field is removed, respectively. Ideal soft magnets for electric motors minimize coercivity and maximize remanence. An example plot of the results can be seen in Figure 27 and Table 8; this shows the total data collected for

each toroid before the selection of cores was made for further testing. The full test data for all toroids can be found in the appendix as Table 2a.

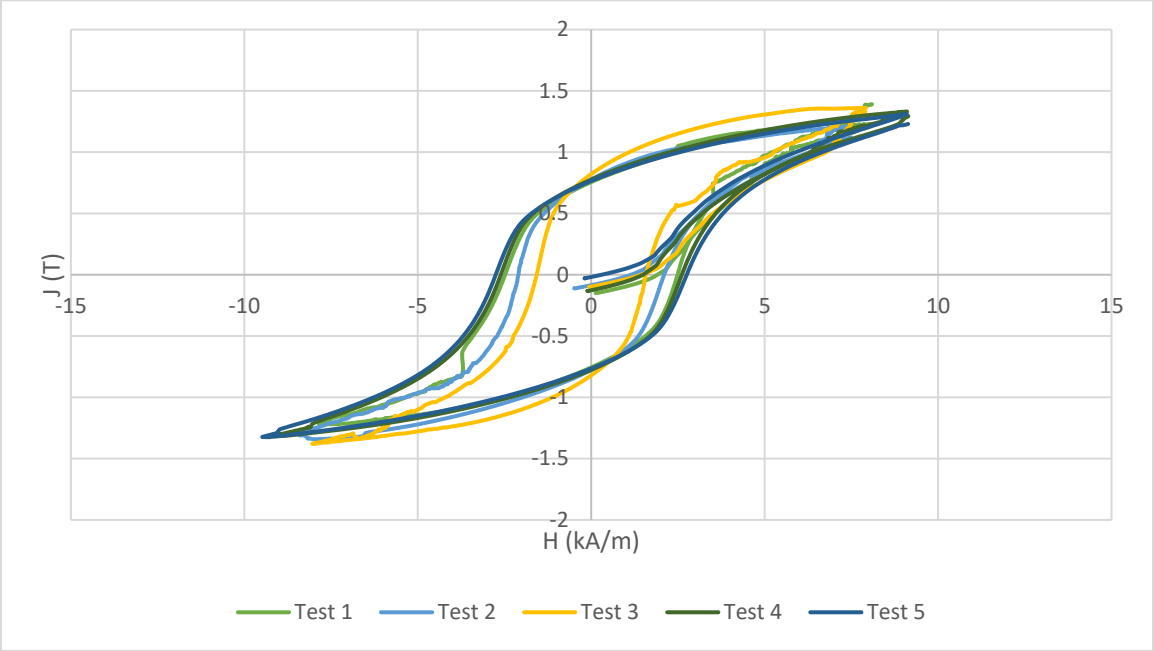

Figure 27: B-H Plot of an Unfocused Beam As-Built Core (UAB-1)

Table 8: B-H intercepts of an Unfocused Beam As-Built Core (UAB-1)

Test #	1	2	3	4	5
Br [T]	0.756	0.778	0.821	0.776	0.765
HcB [kA/m]	2.5	2.1	1.6	2.6	2.7
HcJ [kA/m]	2.5	2.1	1.6	2.6	2.8

Once all cores were wound and tested, cores that were unable to generate a full B-H curve were selected to be subjected to a full *surface* sanding since electrical shorts from surface roughness are the most likely cause of this type of failure. Along with these samples, the first core from each treatment was selected for *edge* sanding. Testing these two samples side by side would indicate whether the surface roughness of a toroid caused the shorting, or if the sharp edges left behind by the wire EDM cutting were the cause of the odd hysteresis plots observed. Figure 28

below shows the impact of both sanding methods on a heat-treated core; there was a large improvement in both sanded cores when compared to its as-built counterpart. The test data for these cores is available in the appendix as Table 3a. This relatively small observable difference between the two processing methods led to the selection of sanded edge cores as the method of processing to investigate, as sanding the entire surface of an AM part might not be a feasible option depending on part geometry.

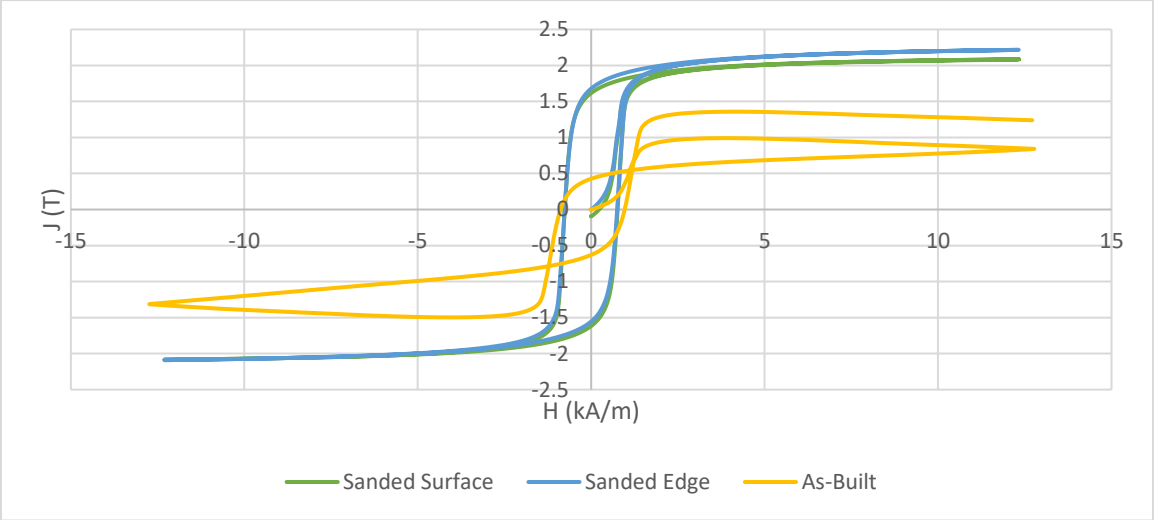

Figure 28: Improvement from Shorted As-Built Core, to Sanded Edge, and Fully Sanded (UAB-4)

Table 9 shows the final results for the AM-produced toroids. These rings were tested two times, wound initially with no post processing after cutting, and then rewound with their sharp edges sanded down to reduce the chance of shorting. The magnetic/mechanical anneal column shows the expected values for Hiperco 50 as described by the manufacturer.

Table 9: Magnetic Results Table

Beam Status	Processing	Edges	Br [T]	HcB [kA/m]	HcJ [kA/m]	u [H/m]	Relative u
Focused	As-Built	As-Cut	0.722	2.426	2.431	0.000298	236.773
		Sanded	0.937	1.582	1.584	0.000593	471.509
	Heat-Treated	As-Cut	1.219	1.860	1.861	0.000655	521.496
		Sanded	1.386	0.785	0.785	0.001766	1405.362
Unfocused	As-Built	As-Cut	0.765	2.748	2.753	0.000278	221.519
		Sanded	0.752	1.260	1.261	0.000597	475.268
	Heat-Treated	As-Cut	0.528	0.923	0.923	0.000573	455.680
		Sanded	1.617	0.756	0.756	0.002139	1701.799
Rolled Standard			1.698	0.181	0.181	0.009394	7475.776
Mag/Mech Anneal			2.3/2.3	0.04/0.125	0.04/0.125	0.0241/0.0099	19200/7900

These results indicate that while heat treatment and post processing can improve the remanence and coercivity greatly, they are still much worse than the rolled parts. The best performing treatment was the unfocused beam, heat treated, with sanded edges, although it still retained 30% less of the applied field (remanence) while requiring 5-18 times the applied field to achieve the same result. This table also shows that none of the specimens approached the relative permeability of either magnetically or mechanically heat treated rolled Hiperco 50, being an order of magnitude lower than the magnetic treatment in the best case. Figures 29 and 30 below show the impact that different parameters have on the resulting magnetic properties. Figure 30 shows the raw toroids with no post processing, the rough edges of the FHT loop, and odd shape of the UHT loop. These are indications that shorting has occurred in the windings, and their drastic change in shape in Figure 30 confirms this, bringing the curves into much more expected shapes. Unfortunately, the large area under all of these curves is indicative of high core losses as well, both before and after sanding.

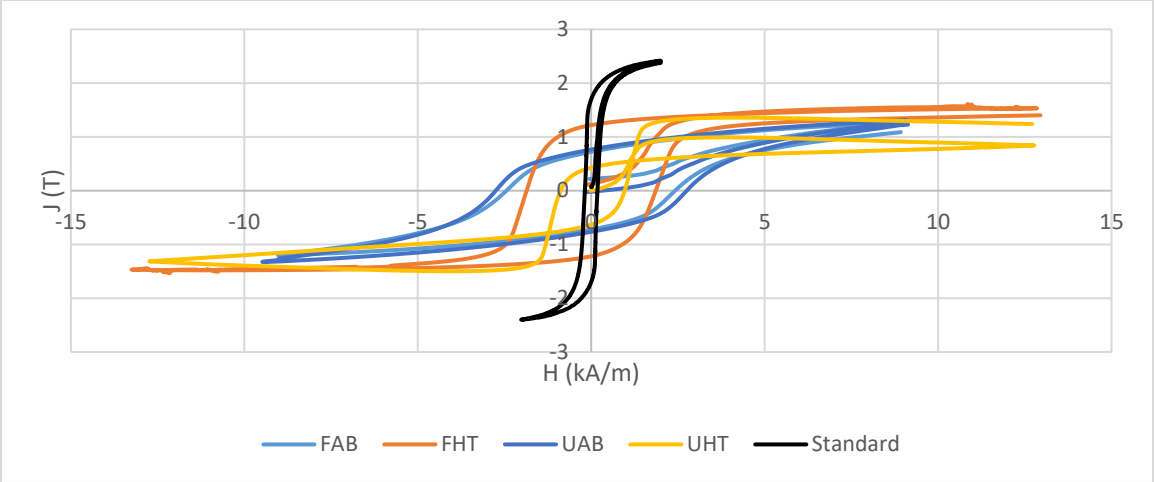

Figure 29: B-H Plot for As-Cut Condition

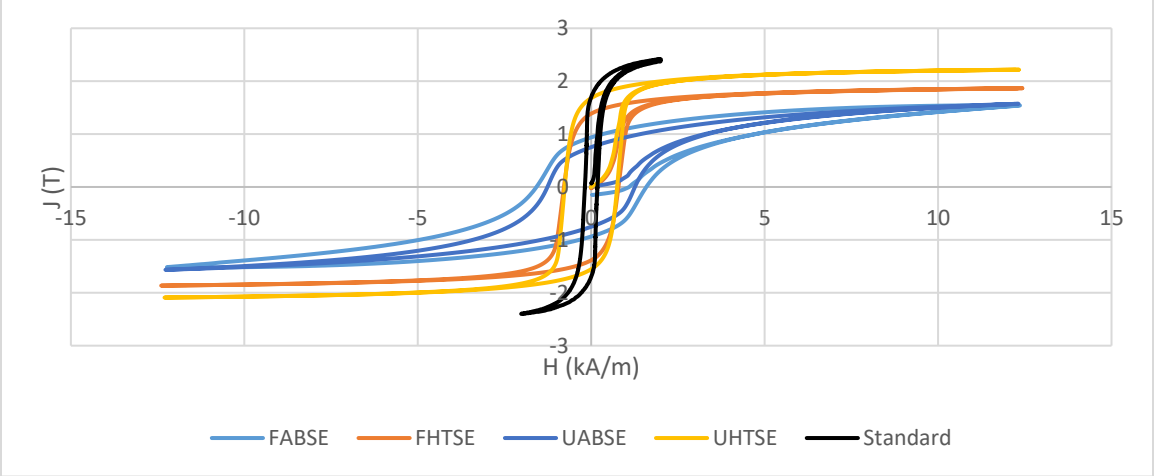

Figure 30: B-H Plot for Sanded Edge Samples

CHAPTER 5

CONCLUSION AND RECOMMENDATIONS

5.1 CONCLUSION

Overall, this project has shown that SLM still has serious hurdles to overcome before it becomes materially and economically viable to produce magnetic Hiperco 50 components. In addition to the expected issues with porosity and density, there were unexpected difficulties in manufacturing, mechanical strength, and the magnetic properties of the final parts.

While the problems with porosity and density were expected, the magnitude of the impact was not. By pulling the beam 2mm out of focus and keeping other parameters constant there was a significant improvement in all metrics measured here. While part of this difference could be explained by the clogging of an airflow sensor during the focused beam build (thus changing the temperature and atmosphere in the build chamber), some test specimens were unaffected by this error. The blockage occurred approximately halfway up the total build height, thus could explain the mechanical weakness of the focused vertical specimens, but the toroids from above this line are indistinguishable in performance from their lower counterparts. Additionally, the density cubes which were all built below this line show a 5% reduction in density and a 2-4% increase in pore area when compared to their unfocused counterparts. In the porosity images there are indicators that some of the powder wasn't completely melted during the build, namely circular protrusions into pores in the size range of the powder.

It was difficult to observe any grain structure in the as-built specimens, but the areas of possible grains observed were of similar size to the visible grains post heat treatment and also maintained similar size regardless of orientation. This indicates that the grains formed during the build are equiaxial and should not contribute to the anisotropy observed in the mechanical testing. The observed anisotropy is most likely from the weaker layer to layer bonding along the melt pools, though the melt pools themselves were not visible in grain structure analysis. Inspection of the grain structure also revealed niobium precipitates in the grain boundary regions which could further contribute to the mechanical weakness of the heat-treated specimens. It follows that the more brittle crystalline failure surface of the heat-treated specimens could be due to the weakening of the grain boundaries caused by these precipitates. However, before heat treatment the unfocused specimens exhibited a surprisingly ductile failure mode, though this was not shown to be of a greater magnitude than can be expected from rolled Hiperco 50 parts.

Continuing the trend of decreased performance from rolled the magnetic properties also suffered in the AM Hiperco builds. All specimens showed higher coercivity, lower remanence, and lower permeability than rolled Hiperco, though the heat treatment process did improve the performance. All tested cores required a larger input field to produce a smaller output field, and additionally required more effort to be demagnetized, making them an overall poor choice for electric motor cores.

The one concern not directly addressed in this report that is a considerable hurdle to using AM techniques on a larger scale is the cost differential between AM components and traditionally manufactured components. During the build process it was estimated that for the time using the machine with the powder provided, that each 3” tall build plate would cost roughly $10,000, it was also estimated that the cost to cut the 3” test stator on the build plate into .007” thick laminations would also cost approximately $10,000 and take around 50 man hours on a wire EDM. Additionally, to wind the core there needs to be some degree of post processing completed

to preserve the magnet wire insulation and prevent shorts, which is an additional cost in man hours. The commercial motor that inspired this work comes complete, off the shelf for $300, but to replicate it using this approach that same motor would cost over $20,000. Unless being used for a novel design where traditional production methods are impossible and the loss in performance described here is acceptable, current practices offer a much better solution to motor manufacturing.

5.2 RECOMMENDATIONS FOR FUTURE WORK

While the results from this initial study seem bleak, there is certainly room for further study into using AM processes to build magnetic components. The first recommendation would be to increase the depth of study for the grain structure of both as built and heat-treated specimens. The methods applied above had great difficulty in establishing a structure for the as-built state, though the heat-treated state was much more visible. The first area of interest would be imaging the surface of each specimen as a EBSD grain map, which could hopefully improve the clarity by showing different orientations of the grains as well. This could be used to establish a link to the orientation of the build direction as well which may influence the observed mechanical anisotropy.

The next area of interest for future work would be expanding the scope of the heat treatments applied to the specimens. Since these samples were outsourced and time was a factor in completion a full test grid was not created and only the manufacturer recommendation for magnetic properties was used. It would be prudent to expand this study as the starting stock was of much poorer quality when compared to the rolled stock this treatment was designed for. A longer treatment may do a better job of closing the pores present and varying the cooling rates may impact how brittle the final specimen is.

The final recommendation would be to directly investigate the impact of changing build parameters between layers on magnetic properties. If it could be shown that different build qualities could insulate magnetic layers enough to not require lamination, then whole magnetic cores could be built, greatly reducing the cost, time, and effort of post processing. This would first necessitate the perfection of parameters for a core material without the need for a finishing heat treatment. The small final differences in the hysteresis loops between the focused and unfocused cores (in both their as-built and heat treated states) indicate that this may be impossible without severely damaging the mechanical properties to create vast differences in the properties between layers. An alternative method may be to alternate material between layers; however, this produces its own challenges in layer to layer bonding. The magnitude of this changing layer to layer bonding would also need to be quantified, but the requirement for mechanical strength is relatively low in the non-load bearing motor cores.

REFERENCES

1. Cullity, B. D., and C. D. Graham. *Introduction to Magnetic Materials*. 2nd ed., Wiley-IEEE Press, 2008.
2. Callister, William Jr., and David Rethwisch. *Materials Science and Engineering: An Introduction*. 9th ed., Wiley, 2013.
3. Wijn, Henricus. *Ferromagnetism / Ferromagnetismus (Handbuch Der Physik Encyclopedia of Physics, 4 / 18 / 2) (English and German Edition)*. Softcover reprint of the original 1st ed. 1966, Springer, 2013.
4. Shiozaki, M., Kurosaki, Y. The effects of grain size on the magnetic properties of nonoriented electrical steel sheets. J. Materials Engineering 11, 37–43 (1989). https://doi.org/10.1007/BF02833752
5. Dirk Herzog, Vanessa Seyda, Eric Wycisk, Claus Emmelmann, Additive manufacturing of metals, Acta Materialia, Volume 117, 2016, Pages 371-392, ISSN 1359-6454, https://doi.org/10.1016/j.actamat.2016.07.019.
6. S. Urbanek et al., "Additive Manufacturing of a Soft Magnetic Rotor Active Part and Shaft for a Permanent Magnet Synchronous Machine," 2018 IEEE Transportation Electrification Conference and Expo (ITEC), 2018, pp. 668-674, doi: 10.1109/ITEC.2018.8450250.
7. Scipioni Bertoli, Umberto & Wolfer, Alexander & Matthews, Manyalibo & Delplanque, Jean-Pierre & Schoenung, Julie. (2016). On the limitations of Volumetric Energy Density as a design parameter for Selective Laser Melting. Materials & Design. 113. 10.1016/j.matdes.2016.10.037.
8. Pavel Hanzl, Miroslav Zetek, Tomáš Bakša, Tomáš Kroupa, The Influence of Processing Parameters on the Mechanical Properties of SLM Parts, Procedia Engineering, Volume

100, 2015, Pages 1405-1413, ISSN 1877-7058, https://doi.org/10.1016/j.proeng.2015.01.510.

9. I. Yadroitsev, P. Krakhmalev, I. Yadroitsava, Hierarchical design principles of selective laser melting for high quality metallic objects, Additive Manufacturing, Volume 7, 2015, Pages 45-56, ISSN 2214-8604, https://doi.org/10.1016/j.addma.2014.12.007.
10. Mikler, C. V., Chaudhary, V., Borkar, T., Soni, V., Jaeger, D., Chen, X., Contieri, R., Ramanujan, R., Banerjee, R., Laser Additive Manufacturing of Magnetic Materials, JOM: the journal of the Minerals, Metals, & Materials Society, Volume 69, 2017, pages 532-543, ISSN 1543-1851.
11. Frazier, W.E. Metal Additive Manufacturing: A Review. J. of Materi Eng and Perform 23, 1917–1928 (2014). https://doi.org/10.1007/s11665-014-0958-z
12. D. Goll, D. Schuller, G. Martinek, T. Kunert, J. Schurr, C. Sinz, T. Schubert, T. Bernthaler, H. Riegel, G. Schneider, Additive manufacturing of soft magnetic materials and components, Additive Manufacturing, Volume 27, 2019, Pages 428-439, ISSN 2214-8604, https://doi.org/10.1016/j.addma.2019.02.021.
13. Bradley C. Salzbrenner, Jeffrey M. Rodelas, Jonathan D. Madison, Bradley H. Jared, Laura P. Swiler, Yu-Lin Shen, Brad L. Boyce, High-throughput stochastic tensile performance of additively manufactured stainless steel, Journal of Materials Processing Technology, Volume 241, 2017, Pages 1-12, ISSN 0924-0136, https://doi.org/10.1016/j.jmatprotec.2016.10.023.
14. Wu, A.S., Brown, D.W., Kumar, M. et al. An Experimental Investigation into Additive Manufacturing-Induced Residual Stresses in 316L Stainless Steel. Metall Mater Trans A 45, 6260–6270 (2014). https://doi.org/10.1007/s11661-014-2549-x
15. A.A. Deev, P.A. Kuznetcov, S.N. Petrov, Anisotropy of Mechanical Properties and its Correlation with the Structure of the Stainless Steel 316L Produced by the SLM Method,

Physics Procedia, Volume 83, 2016, Pages 789-796, ISSN 1875-3892, https://doi.org/10.1016/j.phpro.2016.08.081.

16. "Soft Magnetic Alloys | Carpenter Electrification." *Carpenter Electrification*, CRS Holdings, Inc., 20 May 2020, www.carpenterelectrification.com/products/soft-magnetic-alloy.
17. D. W. Clegg & R. A. Buckley (1973) The Disorder → Order Transformation in Iron–Cobalt-Based Alloys, Metal Science Journal, 7:1, 48-54, DOI: 10.1179/030634573790445541
18. Pei, Zongrui, Eisenbach, Markus, Mu, Sai, and Stocks, G. Malcolm. Error controlling of the combined Cluster-Expansion and Wang–Landau Monte-Carlo method and its application to FeCo. United States: N. p., 2018. Web. https://doi.org/10.1016/j.cpc.2018.09.017.
19. I. Baker, A review of the mechanical properties of B2 compounds, Materials Science and Engineering: A, Volumes 192–193, Part 1, 1995, Pages 1-13, ISSN 0921-5093, https://doi.org/10.1016/0921-5093(94)03200-9.
20. E.P George, A.N Gubbi, I Baker, L Robertson, Mechanical properties of soft magnetic FeCo alloys, Materials Science and Engineering: A, Volumes 329–331, 2002, Pages 325-333, ISSN 0921-5093, https://doi.org/10.1016/S0921-5093(01)01594-5.
21. Z. Turgut, J. H. Scott, M. Q. Huang, S. A. Majetich, and M. E. McHenry , "Magnetic properties and ordering in C-coated FexCo1−x alloy nanocrystals", Journal of Applied Physics 83, 6468-6470 (1998) https://doi.org/10.1063/1.367922
22. L. Sun, Y. Hao, C. -. Chien and P. C. Searson, "Tuning the properties of magnetic nanowires," in IBM Journal of Research and Development, vol. 49, no. 1, pp. 79-102, Jan. 2005, doi: 10.1147/rd.491.0079.

23. R. S. Sundar & S. C. Deevi (2005) Soft magnetic FeCo alloys: alloy development, processing, and properties, International Materials Reviews, 50:3, 157-192, DOI: 10.1179/174328005X14339
24. Kustas, Andrew B., Susan, Donald F., Johnson, Kyle L., Whetten, Shaun R., Rodriguez, Mark A., Dagel, Daryl J., Michael, Joseph R., Keicher, David M., and Argibay, Nicolas. Characterization of the Fe-Co-1.5V soft ferromagnetic alloy processed by Laser Engineered Net Shaping (LENS). United States: N. p., 2018. Web. https://doi.org/10.1016/j.addma.2018.02.006.
25. Kawahara, K. Effect of additive elements on cold workability in FeCo alloys. J Mater Sci 18, 1709–1718 (1983). https://doi.org/10.1007/BF00542066
26. Lie Zhao, I. Baker, The effect of grain size and Fe:Co ratio on the room temperature yielding of FeCo, Acta Metallurgica et Materialia, Volume 42, Issue 6, 1994, Pages 1953-1958, ISSN 0956-7151, https://doi.org/10.1016/0956-7151(94)90020-5.
27. "Hiperco® 50, Hiperco® 50A & Hiperco® 50 HS Properties." *Ed Fagan Inc.*, 2021, www.edfagan.com/soft-magnetic-alloys/hiperco-50/hiperco-50-50a-50-hs-properties.
28. Kustas, Andrew B., Michael, Joseph R., Susan, Don F., Karaman, Ibrahim, and Jozaghi, Taymaz. Equal channel angular extrusion for bulk processing of Fe–Co–2V soft magnetic alloys, part II: Texture analysis and magnetic properties. United States: N. p., 2018. Web. doi:10.1557/jmr.2018.150.
29. A Duckham, D.Z Zhang, D Liang, V Luzin, R.C Cammarata, R.L Leheny, C.L Chien, T.P Weihs, Temperature dependent mechanical properties of ultra-fine grained FeCo–2V, Acta Materialia, Volume 51, Issue 14, 2003, Pages 4083-4093, ISSN 1359-6454, https://doi.org/10.1016/S1359-6454(03)00228-3.

30. Kustas, Andrew B., Fancher, Chris M., Whetten, Shaun R., Dagel, Daryl J., Michael, Joseph R., and Susan, Donald F. Controlling the extent of atomic ordering in intermetallic alloys through additive manufacturing. United States: N. p., 2019. Web. https://doi.org/10.1016/j.addma.2019.06.020.

31. Babuska, Tomas F., Wilson, Mark A., Johnson, Kyle L., Whetten, Shaun R., Curry, John F., Rodelas, Jeffrey M., Atkinson, Cooper, Lu, Ping, Chandross, Michael, Krick, Brandon A., Michael, Joseph R., Argibay, Nicolas, Susan, Donald F., and Kustas, Andrew B. Achieving high strength and ductility in traditionally brittle soft magnetic intermetallics via additive manufacturing. United States: N. p., 2019. Web. https://doi.org/10.1016/j.actamat.2019.08.044.

32. ASTM Standard D792-00, 2021, "Standard Test Methods for Density and Specific Gravity (Relative Density) of Plastics by Displacement", ASTM International, West Conshohocken, PA, 2021, DOI: 10.1520/D0792-00, www.astm.org.

33. Zhu, Q., et al. "An Increase of Structural Order Parameter in Fe–Co–V Soft Magnetic Alloy after Thermal Aging." *Applied Physics Letters*, vol. 69, no. 25, 1996, pp. 3917–19. *Crossref*, doi:10.1063/1.117569.

APPENDIX A

VOLUME AND MAGNETIC TESTING DATA

Table 1a: Pycnometer Volume Data (all volumes in cm^3)

	Focused			Unfocused		
Specimen	As-Built	Pre-Anneal	Annealed	As-Built	Pre-Anneal	Annealed
1	0.9758	0.9656	0.9512	0.9884	0.9935	0.9962
2	0.9645	0.9857	0.9800	0.9866	0.9864	0.9930
3	0.9776	0.9674	0.9561	0.9859	0.9980	1.0025
4	0.9722	0.9783	0.9672	0.9935	0.9878	0.9895
5	0.9739	0.9760	0.9692	0.9804	0.9836	0.9853

Table 2a: Magnetic Testing Data

Specimen	Property	1	2	3	4	5
FAB-1	**Br [T] =**	0.292	0.366	0.442	0.689	0.722
	HcB [kA/m] =	1.9	2.1	2.1	2.4	2.4
	HcJ [kA/m] =	1.9	2.1	2.2	2.4	2.4
FAB-2	**Br [T] =**	0.815	0.800	0.793	0.778	0.791
	HcB [kA/m] =	1.4	1.3	1.3	1.3	1.3
	HcJ [kA/m] =	1.4	1.3	1.3	1.3	1.3
FAB-3	**Br [T] =**	0.633	0.699	0.785	0.794	0.796
	HcB [kA/m] =	1.4	1.4	1.4	1.4	1.4
	HcJ [kA/m] =	1.4	1.4	1.4	1.4	1.4
FHT-1	**Br [T] =**	0.786	0.939	1.095	1.163	1.219
	HcB [kA/m] =	1.1	1.5	1.5	1.1	1.9
	HcJ [kA/m] =	1.1	1.5	1.5	1.1	1.9
FHT-2	**Br [T] =**	0.327	0.330	0.330	-0.079	X
	HcB [kA/m] =	3.2	3.2	3.2	2.6	X
	HcJ [kA/m] =	3.2	3.2	3.2	2.6	X
FHT-3	**Br [T] =**	0.437	0.460	0.771	0.804	0.814
	HcB [kA/m] =	4.4	4.4	5.7	5.8	6.1
	HcJ [kA/m] =	4.4	4.5	5.7	5.8	6.1
FHT-4	**Br [T] =**	-0.067	X	X	X	X
	HcB [kA/m] =	0.8	X	X	X	X
	HcJ [kA/m] =	0.9	X	X	X	X
UAB-1	**Br [T] =**	0.76	0.78	0.82	0.78	0.76
	HcB [kA/m] =	2.48	2.10	1.57	2.60	2.75
	HcJ [kA/m] =	2.49	2.10	1.57	2.61	2.75
UAB-2	**Br [T] =**	0.901	0.901	0.908	0.915	0.913
	HcB [kA/m] =	2.1	2.1	2.1	2.1	2.1
	HcJ [kA/m] =	2.1	2.1	2.1	2.1	2.1
UAB-3	**Br [T] =**	1.194	1.128	1.159	1.176	1.176
	HcB [kA/m] =	2.4	2.3	2.4	2.3	2.0
	HcJ [kA/m] =	2.4	2.3	2.4	2.3	2.0
UHT-1	**Br [T] =**	0.468	0.512	0.552	0.435	0.528
	HcB [kA/m] =	1.0	1.0	1.0	0.9	0.9
	HcJ [kA/m] =	1.0	1.0	1.0	0.9	0.9
UHT-2	**Br [T] =**	0.696	0.655	0.653	0.805	X
	HcB [kA/m] =	4.8	2.8	2.8	2.9	X
	HcJ [kA/m] =	4.8	2.8	2.8	2.9	X
UHT-3	**Br [T] =**	X	X	X	X	X
	HcB [kA/m] =	X	X	X	X	X
	HcJ [kA/m] =	X	X	X	X	X
UHT-4	**Br [T] =**	0.696	0.728	0.774	0.630	0.487
	HcB [kA/m] =	4.8	4.7	4.5	5.0	4.6
	HcJ [kA/m] =	4.8	4.7	4.6	5.0	4.6

Table 3a: Magnetic Post-Processing Testing Data

Specimen	Property	1	2	3	4	5
FABSE-1	**Br [T] =**	0.821	0.824	0.825	0.920	0.937
	HcB [kA/m] =	1.4	1.5	1.5	1.6	1.6
	HcJ [kA/m] =	1.4	1.5	1.5	1.6	1.6
FHTSE-1	**Br [T] =**	1.392	1.393	1.390	1.390	1.386
	HcB [kA/m] =	0.8	0.8	0.8	0.8	0.8
	HcJ [kA/m] =	0.8	0.8	0.8	0.8	0.8
UABSE-1	**Br [T] =**	0.744	0.742	0.742	0.755	0.752
	HcB [kA/m] =	1.3	1.3	1.3	1.3	1.3
	HcJ [kA/m] =	1.3	1.3	1.3	1.3	1.3
UABSE-2	**Br [T] =**	1.629	1.626	1.625	1.622	1.617
	HcB [kA/m] =	0.8	0.8	0.8	0.8	0.8
	HcJ [kA/m] =	0.8	0.8	0.8	0.8	0.8
FHTS-4	**Br [T] =**	0.980	0.982	0.978	1.041	1.070
	HcB [kA/m] =	0.8	0.8	0.8	0.8	0.9
	HcJ [kA/m] =	0.8	0.8	0.8	0.8	0.9
UHTS-3	**Br [T] =**	1.628	1.625	1.624	1.621	1.617
	HcB [kA/m] =	0.8	0.8	0.8	0.8	0.8
	HcJ [kA/m] =	0.8	0.8	0.8	0.8	0.8